Assuring Integrity of CO_2 storage sites through ground surface monitoring (SENSE)

Deliverable No.:	Final Report (D1.1 to D5.3)	Responsible for deliverable:	Norwegian Geotechnical Institute (NGI)
Quality control by:	NGI	Contributing partner(s):	NGI, BGS, GEOMAR, IFPEN, CIUDEN, LLNL, UiO, IGME, RITE, CSIRO, KIGAM, UT Austin, Quad Geometrics
Deliverable prepared by:	Bahman Bohloli, Joonsang Park, Per Sparrevik, Malte Vöge, Nazmul H. Mondol, Ola Eiken, White Joshua, Ceri Vincent, Juan Andrés Marín Vidal, Almudena Sanchez de la Muela, José Francisco Mediato Arribas, Christian Berndt, Jens Karstens, Sarah Bouquet, Ziqiu Xue, Saeed Salimzadeh, Elaheh Arjomand, Yong-Chan Park, Yeon-Kyeong Lee, Md. Jamilur Rahman	Dissemination level:	Public
Project No.:	299664	Date:	25/04/2023

This project, SENSE, is funded through the ACT programme (Accelerating CCS Technologies, Horizon2020 Project No 294766). Financial contributions made from; The Research Council of Norway, (RCN), Norway, Gassnova SF (GN), Norway, Bundesministerium für Wirtschaft und Energie (BMWi), Germany, French Environment & Energy Management Agency (ADEME), France, US-Department of Energy (US-DOE), USA, Department for Business, Energy & Industrial Strategy (BEIS) together with extra funding from NERC and EPSRC research councils, United Kingdom, Agencia Estatal de Investigación (AEI), Spain, and Equinor, Quad Geometrics are gratefully acknowledged.

Project information

Project title:	Assuring integrity of CO_2 storage sites through ground surface monitoring (SENSE)
Project period:	1 September 2019 - 31 December 2022
Project Coordinator:	Norwegian Geotechnical Institute
Web-site:	https://sense-act.eu/

Project partners

Funding Agencies

Contents

Title Page

ABSTRACT

Injection of CO_2 increases reservoir pressure to some extent depending on permeability and accessible volume of the reservoir. Excess pressure reduces effective stresses and generates formation expansion. This deformation will mainly occur in the reservoir but will also transfer to the surrounding layers. This pressure increase may show up as uplift at the surface or seabed. In this study, we analysed ground uplift owing to CO_2 and gas injections at several sites and developed tools and methods for measuring such deformation. Scale of deformation is likely to be in the range of a few millimeters. Interpretation of the data was used to assess performance of the reservoir and behaviour of faults and fractures throughout the injection and post-injection period. The ultimate goal is to understand the performance of the storage reservoir and seal integrity using measurement of ground uplift combined with geomechanical modelling.

We used seven cases from large scale lab tests to full scale injection sites. The lab tests, carried out in Oslo (Norway) and in Kyoto (Japan), focused on the advancements of Distributed Strain Sensing (DSS) fiber optic cables to measure strain in the range of a few micro-strains (1 micro-strain = 1 micrometre strain per metre of fibre) in a direction perpendicular to the fibre cable axis. We carried out similar experiments in a real offshore environment at Boknis Eck, offshore Germany, to measure seabed uplift with a series of artificial "seabed uplift" tests. Furthermore, In Salah CO_2 storage site (Algeria), Hatfield Moors natural gas storage (onshore UK- as a proxy to CO_2 storage), and Hontomin CO_2 injection test site (Spain) were used for studying ground deformation and understanding its relationship to the subsurface injection of fluids. These test cases used satellite Interferometric Synthetic Aperture Radar (InSAR) to monitor ground movement. The findings and concepts from these case studies were utilized for modelling CO_2 injection and expected ground uplift for High Island 24L, Gulf of Mexico. Analytical solutions and geomechanical modelling approaches were also developed to calculate ground uplift based on pressure disturbances in the subsurface.

The experiments showed that DSS fiber optic cables trenched and laid down horizontally can detect deformation (uplift) of the ground that is greater than of about 5 micro-strain. We also observed that when the cable is trenched to a depth of about 0.5 m, friction between the soil and cable is sufficient to follow actual soil deformation and therefore additional anchors to improve the coupling of the cable to the ground are not required. Another set of experiments showed that DSS cable exhibit a stronger coupling to the ground if it is trenched and covered by cement instead of soil. Full scale experiments in offshore area also concluded that uplift of the seabed can be detected with DSS cable if it is greater than few micro-strain.

The UK case study site, Hatfield Moors gas storage site, was assessed using a combination of techniques and data. Seismic and well data were used to assess the deep geology and build a static model from the base of the reservoir to the ground surface. Numerical flow modelling was undertaken to understand fluid movement and pressure within the storage complex. Geomechanical modelling was undertaken to predict how much surface movement would be expected based on the pressure changes within the reservoir. Additionally, processing and interpretation of InSAR data were used to assess surface movement in light of the model predictions. Modelling results and observed data provided a good match. Key learnings from this study show that flow and geomechanical modelling have a key role to play in understanding fluid (gas/CO_2) storage site behaviour and demonstrate the value of history matching to provide confidence in predicting site behaviour. These modelling results could be used to consider how much ground movement would be expected at any particular site, and therefore the role for ground motion detection in the monitoring programme.

The well-known Geertsma solution for calculating ground uplift based on the reservoir pressure change was modified to a Generalized Geertsma (GG) solution that provides a fast and accurate solution for estimating ground uplift for reservoir and surrounding layers. Results showed that the GG analytical solution gives the same accuracy as the numerical software COMSOL Multiphysics. Geomechanical modelling demonstrated that elastic parameters and permeability of reservoir rock and overlying formations play a crucial role in the magnitude of ground deformation. Furthermore, permeability of faults and fracture zones affects the magnitude of uplift; where sealing faults increase magnitude while leaking faults decrease ground uplift. It also showed that it is important to consider topography of reservoir and overburden in the models as this also affects the magnitude of uplift.

The results of the SENSE project show ground deformation is a parameter that can easily be calculated and monitored onshore and offshore. For onshore sites, satellite data and tiltmeter measurements provide accurate information with a reasonable cost when deformation velocity is in the range of about 3 millimeters per year or greater. We advanced a procedure for automatic processing of InSAR data which makes the use of ground deformation for understanding site behaviour onshore even more cost-efficient. For offshore cases DSS fiber optic cables can obtain high resolution seabed uplift data when deployed horizontally in shallow trenches. Use of DSS fibers can be particularly beneficial if there are expected deformation 'hot-spots'. Pattern and shape of ground deformation at surface reveals behavior of the storage complex. For instance, similar and equal uplift on both sides of a fault indicates that the fault is permeable while the opposite implies that the fault might be sealed.

Keywords: CO_2 storage, Monitoring, In Salah, Hatfield Moors, Hontomin, High Island, Boknis Eck, Ground deformation, Strain sensing, Fiber optics, Geertsma solution.

Introduction

Large-scale permanent storage of CO_2 in saline aquifers or depleted hydrocarbon reservoirs has a key role to play in achieving the Paris Climate Accords with the aim of keeping the average global temperature rise below 2°C by 2050. However, injecting fluids into the subsurface has potential geomechanical consequences. A rapid increase of injection induced reservoir pressure could induce significant changes in stress and strain fields within the reservoir, which may then propagate to surrounding layers and cause deformations in sealing layers or reactivation of existing fractures (Davies et al., 2013; Hawkes et al., 2005; Herwanger and Koutsabeloulis, 2011; Jimenez and Chalaturnyk, 2002; Nordbotten et al., 2004; Rutqvist et al., 2008, 2007; Rutqvist and Tsang, 2002; Soltanzadeh and Hawkes, 2008; Streit and Hillis, 2001; Verdon et al., 2013).

Quite often, increase of reservoir pressure causes deformations that can be observed at the surface as heave (Bohloli et al., 2018). Then, by measuring and inverting the observed surface deformation, one can interpolate what has happened in the subsurface. However, the process is quite complex to analyze, and the fully-coupled hydro-mechanics should be taken into account (Bjørnarå et al., 2018). An analytical model such as the Geertsma solution (Geertsma, 1973) can also be used to approximate ground deformation owing to pressure change in the subsurface. The standard Geertsma solution has some assumptions and limitations; 1) the subsurface is an isotropic homogeneous half space; 2) the pressure anomaly should be of infinitely-thin disk shape, and 3) the number of subsurface layers limited to three. Approximation might simplify the model, but this method is quick compared to time-consuming and resource-heavy numerical solutions and a remarkable advancement to overcome those practical limitations (van Opstal 1974, Du and Olson 2001, Tempone et al. 2010, Fokker and Orlic 2006, Mehrabian and Abousleiman 2015). SENSE

project introduced a generalized Geertsma-type solution that has overcome the limitations mentioned above.

Ground deformation can reveal the fluid migration and can be monitored both downhole and at the surface. There are various monitoring methods that target different aspects of a site, such as pressure gauges that give information about near-well areas and can detect the failure of rock based on pressure drop, microseismic monitoring that provides information about possible formation failures, etc. However, monitoring methods that can provide continuous data over long time periods and at feasible costs while also monitoring large volumes are rather limited.

The SENSE project focuses on cost-effective and reliable monitoring techniques for secure subsurface CO_2 storage. The hypothesis is that ground deformation will be observable at surface or seabed and can be translated to understand the performance of the CO_2 storage complex during the injection and post-closure phases. The SENSE project has developed cost-effective approaches, techniques, and tools to monitor ground deformation over large areas and expected deformation 'hot-spots'. We generalized the Geertsma-type solution framework of Mehrabian and Abousleiman (2015) by addressing the vertically-transverse isotropic (VTI) medium modelling. It both generalises the Geertsma solution while also enabling calculation for any number of layers and a finite-thickness disk pressure (Park et al. 2021). In addition, for comparative analysis, advanced but time-consuming numerical solutions were also developed. Ground surface deformation combined with analytical solutions, geomechanical modelling, and inversion provides information on pressure distribution and hydro-mechanical behavior of the CO_2 storage complex that can help operators provide assurance that the storage complex is behaving as expected.

1. Field experiments and case studies

This study presents the development of measurement techniques and modelling concepts based on large-scale experiments, various test sites, and case studies. These cases include both onshore and offshore sites. Oslo field lab (Norway), Kyoto test site (Japan) and Boknis Eck field site (offshore Germany) were used to examine new fiber optics solutions for monitoring strain changes at ground surface caused by artificially induced ground deformation. Hatfield Moors natural gas storage (UK-used as a proxy to CO_2 storage), In Salah CO_2 storage site (Algeria), and Hontomin CO_2 injection test site (Spain), are onshore cases, which offer options for time-lapse monitoring using satellite data (InSAR monitoring). In addition, a Gulf of Mexico case study was used as a hypothetical site to model and estimate seabed deformation owing to the injection of CO_2 to consider which techniques will be most appropriate for monitoring ground deformation if CO_2 is stored there in the future.

For onshore ground deformation monitoring over large spaces, InSAR data provides a cost-efficient option for continuous and long-term monitoring of ground surface movement. For offshore ground deformation, the present state-of-the-art to monitor subsidence utilizes seabed sensors to monitor hydrostatic depth and/or seabed tilt. However, these offshore methods only provide point measurements and data harvesting from self-contained nodes or periodic benchmark surveys are costly. As an alternative approach, monitoring seabed deformations over long baselines by utilizing fiber optic cables for distributed strain sensing (DSS) has been tested and evaluated.

1.1 Oslo sand-box experiment: simulated ground uplift

This experiment was designed to measure artificial uplift of a sand layer and examine the accuracy of fiber optic cables laid down inside the sand measuring ground deformation in the normal direction to cable axis. Sensitivity of axial strain along a Distributed Strain Sensing (DSS) cable is high (±1.0 µstrain). However, quantifying ground uplift based on axial strain measurements is not trivial

and depends on several factors such as cable-soil friction, spatial resolution and the shape of deformations. DSS cables utilized in real-life storage sites must have a mechanical coupling to the ground to monitor the actual seabed uplift (Figure 1.1) but not move due to the currents and scour. Trenching and laying down cables will provide good enough coupling to the ground.

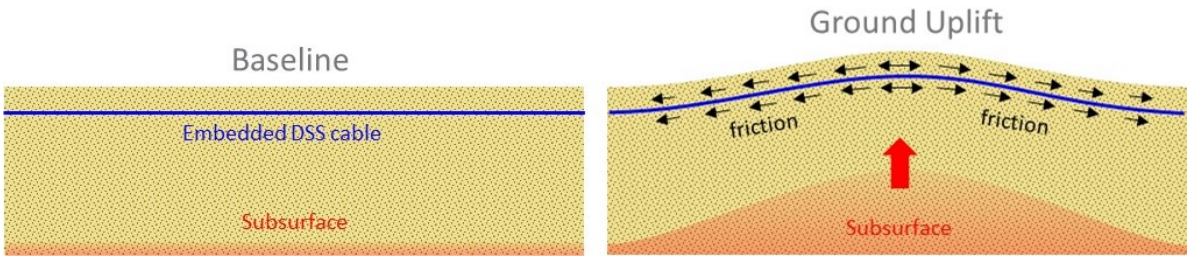

Figure 1.1 The principles for monitoring vertical seabed deformations with embedded DSS cable.

Instead of burying the cable in a trench, the simulated tests were performed in a long "sand box" (Figure 1.2). The bottom could be raised and lowered at three different sections (denoted A, B and C) using airbags beneath 2 m long flexible metal sheet plates. The smooth slope gradients generated by the plates are anticipated as representative for simulating uplift above CO_2 storage sites but, most likely, more difficult to detect by DSS cables than sharp local deformations such as faulting. The true uplift was measured by tell-tale rods connected to the plates at the maximum uplift point, the DSS cables were laid out in the sand layer 100 mm above the plates and finally covered by another 200 mm sand layer simulating cable embedment. No effort was done to pre-tension the cables, only minor hold back was applied to lay out the cables straight along the sand bed. Strain readings with high spatial resolution and several cable configurations were tested including different types of micro anchors along the cables. Robust armoured cables suitable for embedment in the ground with corrugated grip surface and a tight buffered single mode fiber protected inside a central metal tube were used for the tests.

The strain readings were made by Optical Frequency Domain Reflectometry based on Rayleigh backscatter enabling high spatial measuring resolution of interrogated cables at a distance up to 2 km. Multiple tests were performed, each with several uplift increments. The walls of the box and sand surface was vibrated between each test to reconstitute the sand and soil coupling to the DSS cables. The main test objectives were to check the sensitivity of the DSS cables to vertical deformations and establish a correlation between the measured axial strain and the actual uplift. DSS fiber optics readings are sensitive to temperature variations; however, no compensation was required during the test, since the temperature was stable.

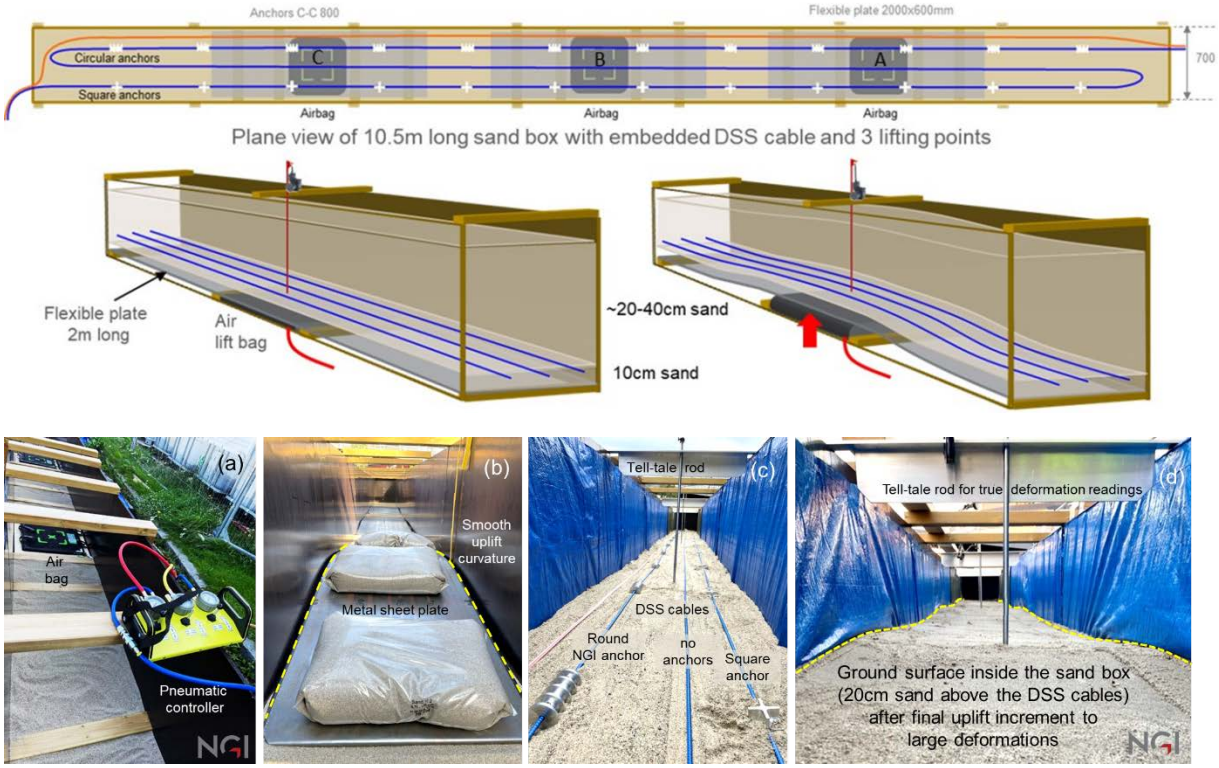

Figure 1.2 The sand box erected for simulated uplift tests using airbags (a) beneath flexible steel sheet plates (b) covered with sand where DSS cables with different micro anchor configurations were laid out (c) and the DSS cables finally covered with 200 mm sand (d).

Test results and observations

Each test series started with a baseline reading since only strain changes relative to a baseline can be recorded by DSS. Typical results from gradually increasing uplift increments for all three arrangements are shown in Figure 1.3. For large uplift the three lifting points (A, B and C) interact and generate increased strain also along the cable sections that remain stationary between the lifting points.

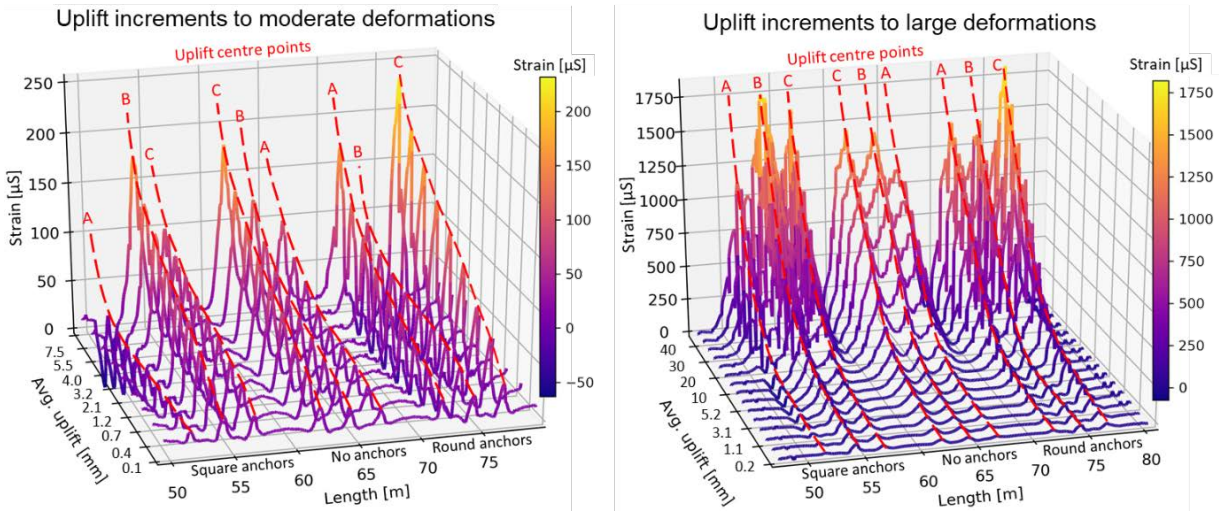

Figure 1.3 Examples of recorded strain response during tests with incremental uplift sequences to moderate (left) and large deformations (right).

Ground surface uplift is a function of excess pressure in storage reservoir. Often, the excess pressure has to be limited due to reactivation of fractures and faults. Therefore, uplift at surface will usually be small when injecting CO_2 at great depths. This indicates the need for high resolution data on strain measurement. A recorded example of the strain response to small uplift increments for the cable without micro anchors is shown in Figure 1.4.

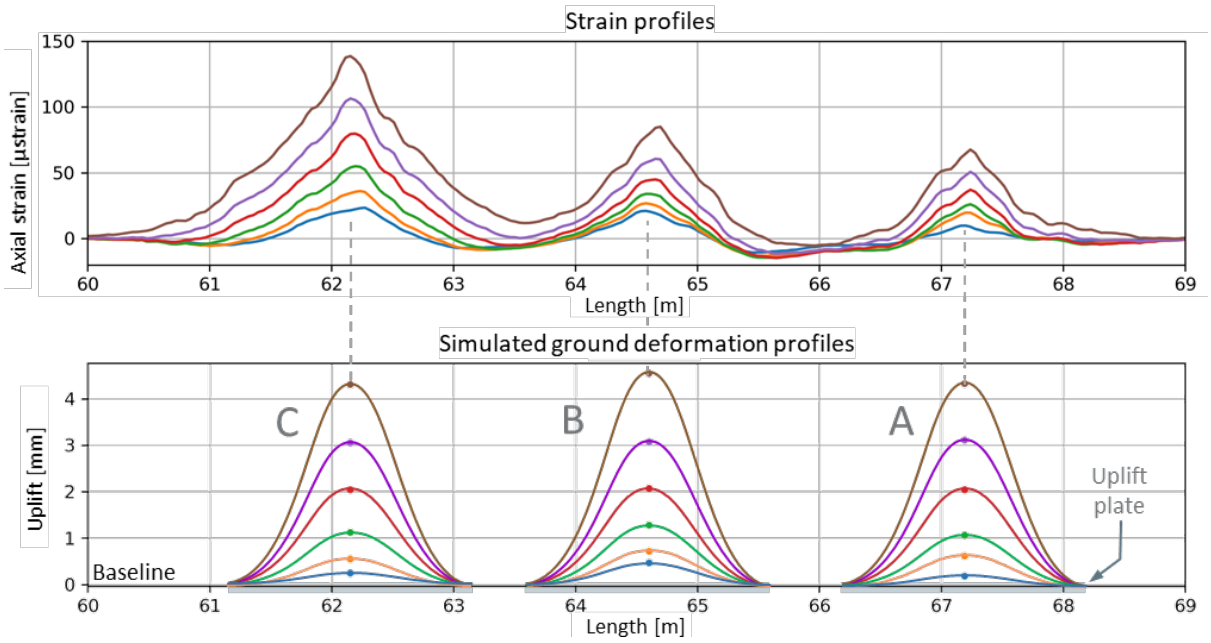

Figure 1.4 Example of strain response and uplift profiles for the DSS cable without micro anchors.

The strain recorded at the highest uplift points has been compiled for all performed tests and examples are plotted in Figure 1.5. As indicated in the plots, high sensitivity is also present for the initial small uplift increments. Uplift of ~0,1mm over 1m length or a slope gradient of 0.01% (minimum applied lift increment) could be clearly observed by the axial strain response in the DSS cable. Cables with micro anchors did not provide any significantly higher sensitivity compared to the bare corrugated cable. The round NGI anchor performed better than the square anchors, which are sensitive to axial rotation (must be carefully placed in the sand), which can affect the axial strain response (less conformity).

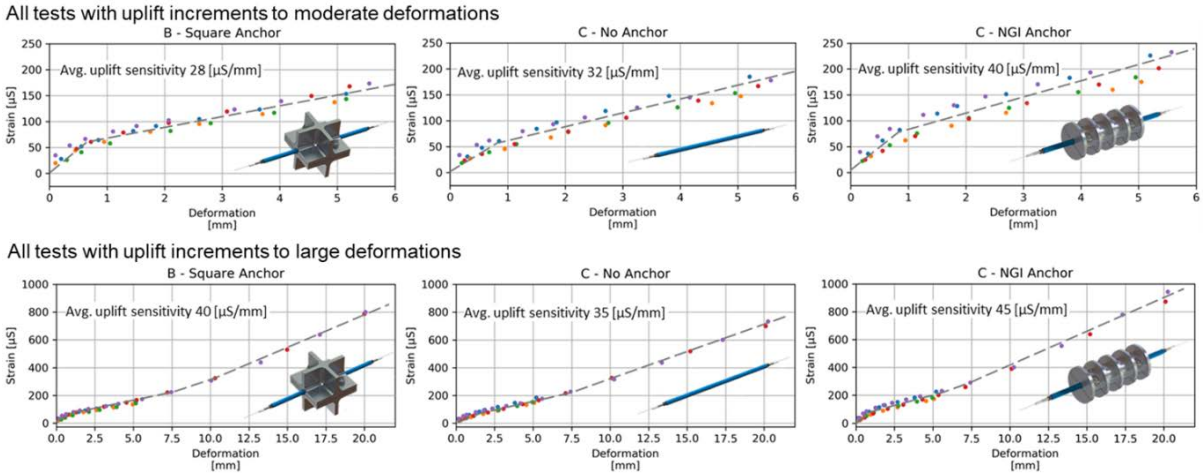

Figure 1.5 Maximum strain versus highest uplift for sections B and C plotted for lifting increments to moderate (top) and large simulated deformations (bottom), the average sensitivities are indicated by dashed lines.

DSS suitability for ground deformation monitoring above CO_2 storage sites

The simulated tests show that the DSS cable can measure the axial strain response with high sensitivity of micro-strain range. To look briefly at the implication of this high sensitivity in a field application, the vertical displacement and horizontal strain are calculated for a homogenous subsurface where elastic modulus, E = 5 GPa, and Poisson's ratio, v = 0.25, subjected to a 100 m thick 1 MPa pressure anomaly with 2500 m radius. The reservoir depth is varied from 500 m to 3000 m and the analytical solution by Park et al. (2021) is implemented. Figure 1.6 shows the calculated results in terms of vertical displacement in (a) and horizontal strain in (b). It is clearly illustrated that the behaviour of vertical displacement and horizontal strain in the subsurface are related to each other, and that continuous measurements along baselines with DSS cables can be beneficial for in-direct monitoring of the vertical displacement in the ground. It is also noted that the apparent sensitivity of the DSS cable is within the range for detection of the deformations derived by this simplified subsurface model. The simplified model does not include the seabed-DSS cable interaction, which, however, has been demonstrated to yield high uplift sensitivity in the performed tests.

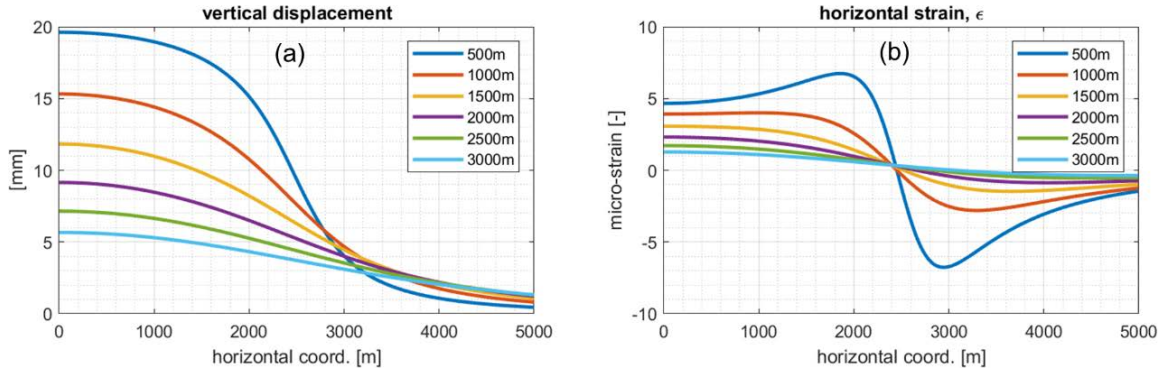

Figure 1.6 Comparison of calculated results for different reservoir depths: (a) vertical displacement [mm] and (b) horizontal strain [µS].

1.2 Ground surface monitoring field tests in Japan

Three field pilot tests were performed for ground surface deformation monitoring using Distributed Fiber Optics Strain Sensing (DFOSS) by installing the fiber cable in a shallow trench excavated at the test site with a total length of 2.9 km and a depth of less than 50 cm (Figure 1.7). Figure 1.7 shows the location of the fiber cable at the test site (green line), along with the locations for three tests at the soil-buried (red) and the cement-covered (black) segments. The iron plates loading test (first test) was performed at both the soil and cement sections for comparison. While the water tank loading (second test) and airbag (third test) tests were carried out only in the cement section. Figure 1.8 shows the single-mode optical fiber cable installation method in the shallow trench for the sections covered by soil and cement, respectively.

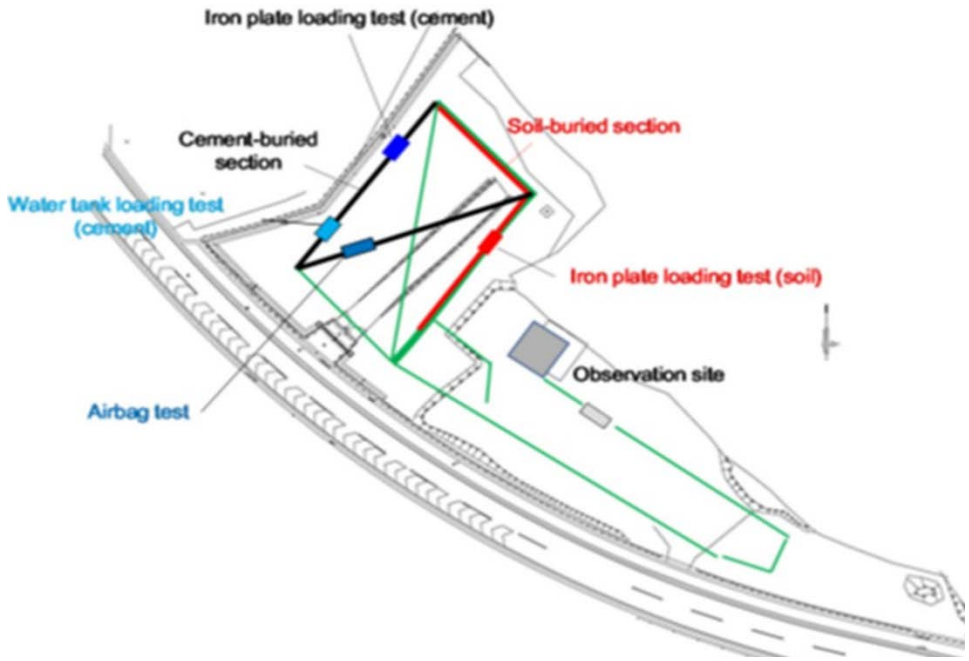

Figure 1.7 Schematic layout of the Distributed Fiber Optics Strain Sensing (DFOSS) cable in Chiba test site, Japan. Colours show different segments of the cable; DFOSS cable (green), soil-buried DFOSS (red) and cement-covered DFOSS (black).

The first test was conducted by applying a static weight load (iron plates) that increased in five stages to reach 12 tons load at the end of the test. The DFOSS response was recorded for both the soil and cement parts to confirm the best method for cable installation. In the second test, the DFOSS response was examined under continuous deformation caused by a dynamic load produced by gradually filling into a water tank placed above the fiber covered by cement. The filling was continued for 6 h and 30 min with a total water capacity of 8 m^3. For the third test, the soil under the cable was excavated, and the DFOSS response to the cavern caused by this process was recorded. Subsequently, two airbags were inserted into the cavern under the fiber cable, and an airbag inflation/deflation experiment was conducted (Figure 1.9). In this experiment, the air pressure in the bag was gradually increased by increasing the air pressure from 25 kPa to 125 kPa in five stages. Then reduced in the same stepwise manner to return to zero, and the DFOSS recorded the deformation for both steps to confirm the ability of DFOSS to monitor uplift and subsidence.

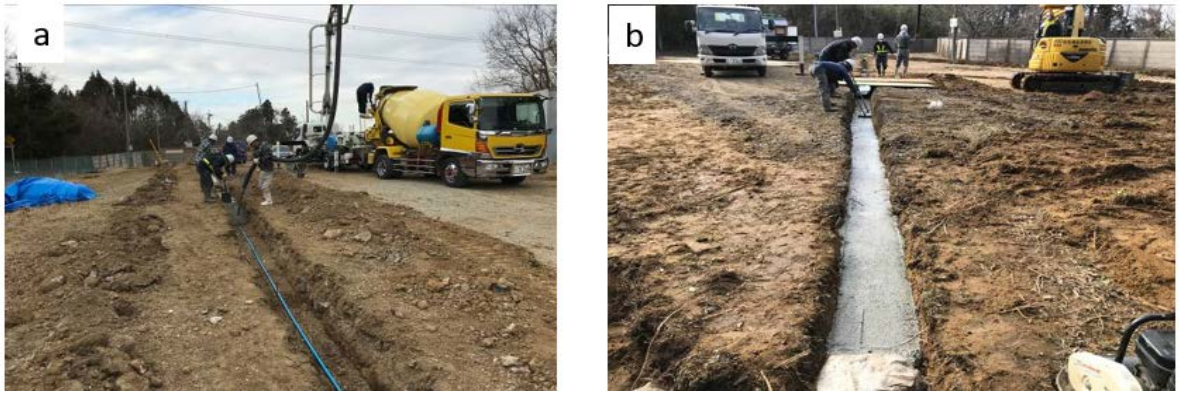

Figure 1.8 Fiber installation methods in the shallow trench: (a) cover with soil, (b) cover with cement.

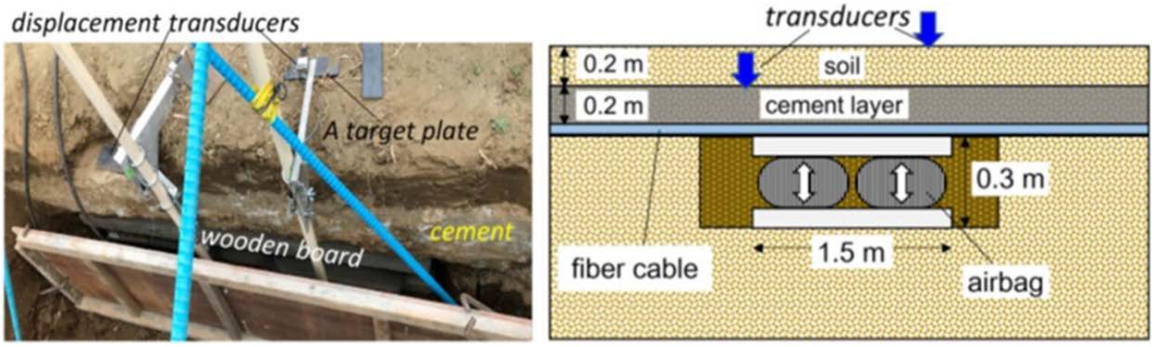

Figure 1.9 Schematics of the airbag tests indicated in Figure 1.7.

Test results and conclusions

Figure 1.10 shows the first static loading test results for the fiber covered with soil (a) and cement (b). The result suggests the weak coupling of the cable with the ground when covered by soil compared with cement. Thus, cement-covered fiber will give a stronger coupling to the ground compared to soil cover. Figure 1.11 shows the results of the second test with a clear deformation profile, with subsidence appearing under the water tank due to the dynamic water filling uploading. Uplift was observed on the two sides. FOSS also detected the uplift caused by increased airbag pressure and the subsidence caused by reduced airbag pressure in the third test (Figure 1.12). These results indicate that DFOSS can be utilized as an accurate ground surface deformation monitoring technology with high spatiotemporal resolution.

The three experiments confirm that DFOSS can monitor ground surface deformation in uplift or subsidence at CO_2 storage or oil and gas production fields. It can also be utilized for structural health monitoring for detecting anomalies and locating their positions along the fiber cable.

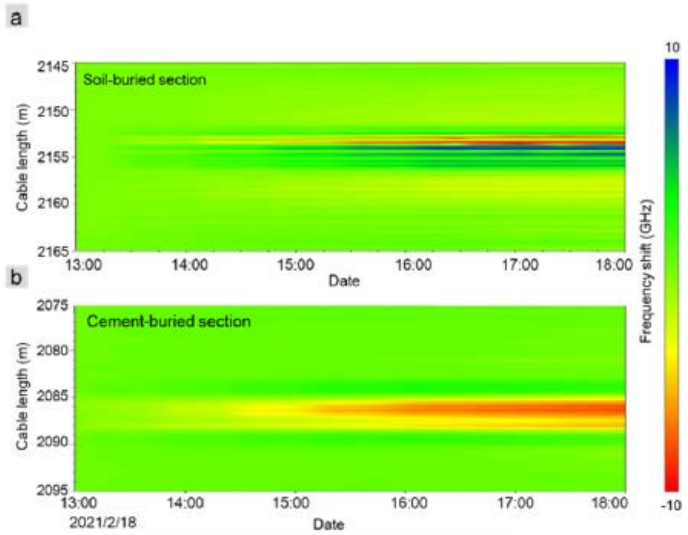

Figure 1.10 Comparison of the spatiotemporal Rayleigh frequency shift response to a static load for the fiber cable covered by soil (a) versus that covered by cement (b). The yellow and red colors indicate ground subsidence, while the blue color indicates ground uplift.

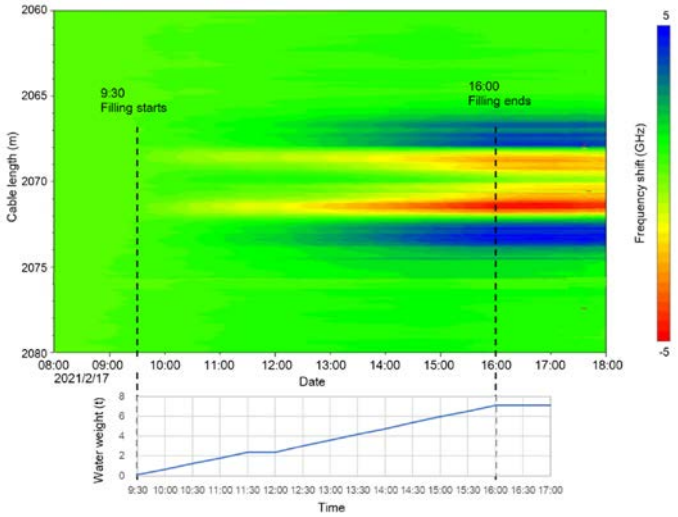

Figure 1.11 Spatiotemporal Rayleigh frequency shift due to dynamic water filling and loading.

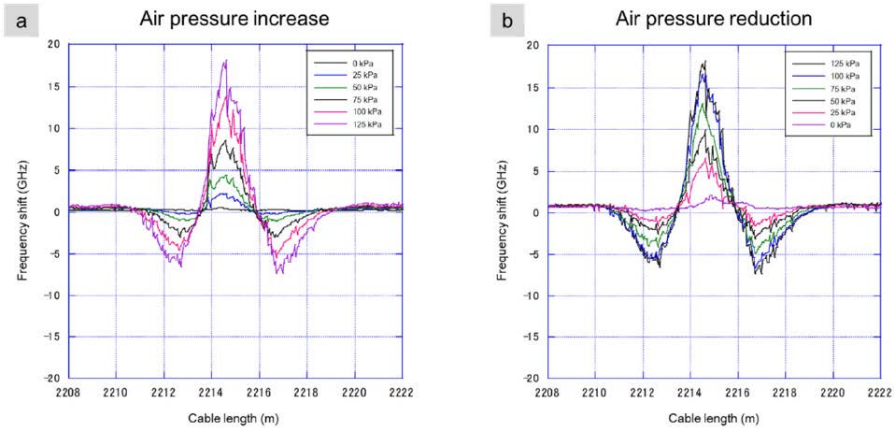

Figure 1.12 Rayleigh frequency shift in response to airbag inflation/deflation experiment. Frequency is proportional to displacement.

1.3 Full scale experiments, Boknis Eck, offshore Germany

To test the general concept of seafloor deformation measurements under real conditions, we performed a field experiment in the Baltic Sea offshore Klein Waabs in an area called Boknis Eck. As injecting air (or other gases) into the underground to cause an uplift of the seafloor was not feasible, we constructed seafloor uplift devices for simulating uplifting and subsidence of the seafloor (Figure 1.13B). To lower the panel, the air is released, while two screws allow a precise and controlled lowering of the device. We built seven of these devices, which were installed by divers. The devices were next to each other on the seafloor approximately 300 m offshore in a water depth of 5 m (Figure 1.13A).

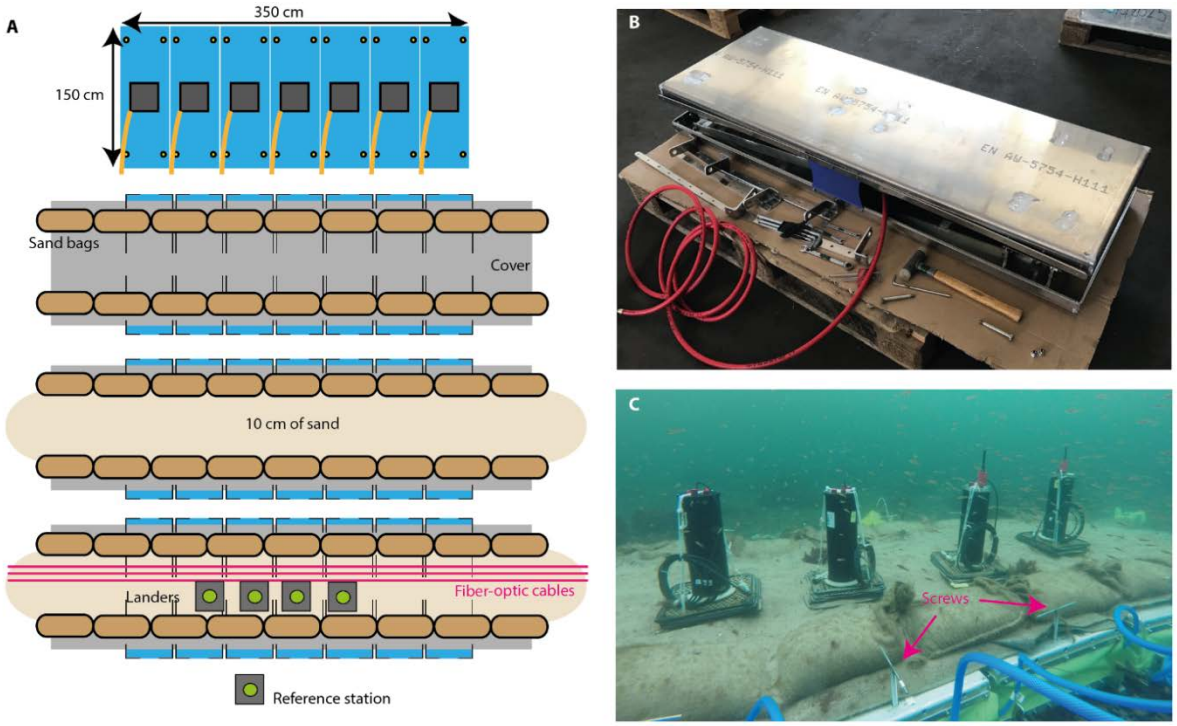

Figure 1.13 A) Measurement setup for the offshore experiments at Boknis Eck consisting of seven pneumatic seafloor uplift devices, three fiber-optic cables and five landers. B) Photograph of a seafloor uplift device. C) Photograph of the measurement setup on the seafloor showing four landers and the screws to manipulate the seafloor uplift devices.

The devices were covered with a fabric cover, with two rows of sand bags forming barriers at their edges and with about 10 cm of sand in between. Three fiber optic cables with a total length of about 600 m each were trenched into this sand cover and connected with a measurement room onshore. For this, the cables needed to cross a public beach, an almost 10 m high cliff and a field (Figure 1.14). In addition, the divers placed four landers equipped with pressure and tilt sensors on top of the sand cover and one reference lander next to it.

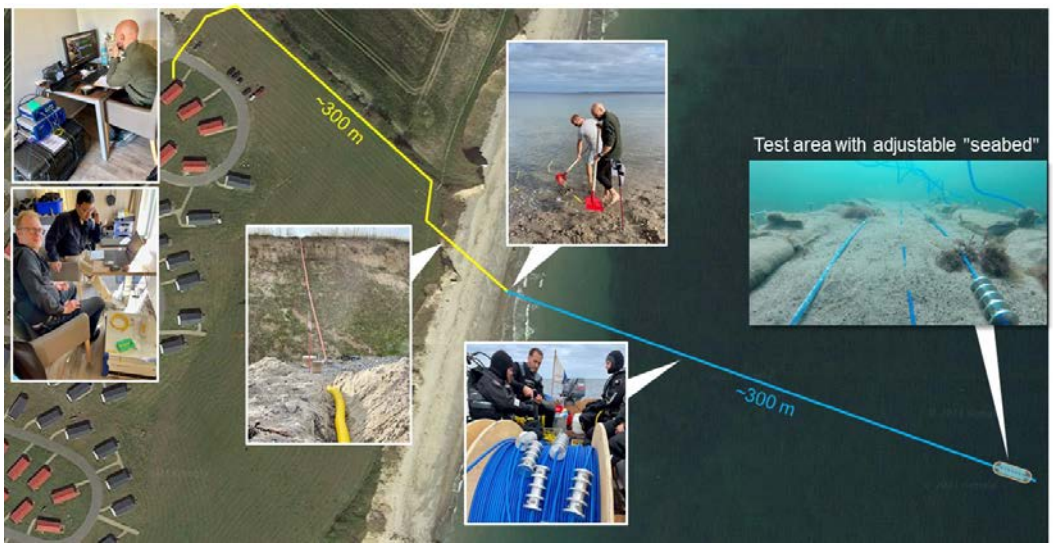

Figure 1.14 Sketch and layout of the field tests in Boknis Eck, offshore Germany.

Instead of simulating uplift by inflating the seafloor devices beginning with a deflated position as default, we decided to measure subsidence and started with a fully inflated position as this movement could be controlled much easier, allowing a more precise control of the system. We performed four measurement cycles with each beginning with all seafloor lift devices being fully inflated and locked in this position by the screws (Figure 1.13C). Then the pressurized air was released and the devices were manually lowered by the divers following previously determined lowering patterns. Figure 1.15 shows the tilt meter measurements from one of these circles for three landers (lander 3 was malfunctioning). The seafloor devices were lowered in 0.25 mm per time step, beginning only with the center panel and later with the two neighbouring panels. Landers 1 and 2 pick up the stepwise increase in tilt, while lander 2 shows a stronger signal as lander 1 as expected due to its position. Lander 4 shows no tilt signal as it is located outside the area of deformation. At the same time the deformation was measured by one of the fiber-optic cables.

Figure 1.15 Absolute tilt recordings during one measurement cycle during the Boknis Eck experiments. The upper panel shows the absolute subsidence during 10 steps of lowering by the divers and the lower panel shows the tilt measurements of three landers during the measurement cycle.

1.4 In Salah CO_2 storage site, Algeria

Onshore ground surface deformation can be estimated using the Interferometric synthetic aperture radar (InSAR) sensor's line-of-sight (LOS) by pairing SAR images capturing the same location from the same position at different times (Figure 1.16). The differential Interferometry SAR (DInSAR) is a specific version of SAR data processing, where two radar images of the same location on the ground are differenced from each other and the topographic phase contribution is removed in order to separate out the phase information caused by radar path delays. This phase information, represented in an interferogram, is used to measure the ground displacement that has taken place between the two captured moments that make the interferogram.

DInSAR is ideal for measuring displacements caused by sudden events like, e.g. earthquakes. The images for the InSAR pair are selected from before and after the event, with as little temporal separation as possible. This ensures good coherence in the interferometric phase. For very slow movements, this technique is not sufficient. The time between acquisitions will either be too short to pick up enough displacement to be detectable, or the timespan will be too long to get a coherent interferometric phase. For these reasons, methods have been developed to process entire timeseries or stacks of SAR images, which allows for the detection and monitoring of comparably small terrain deformations (Figure 1.16). The most widely used methods are the Permanent Scatterer (PS) approach and the Small BAseline Subset (SBAS) approach.

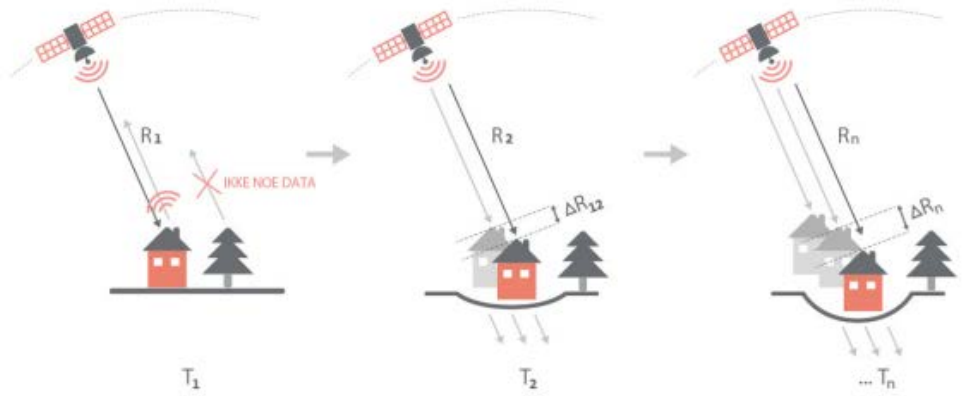

Figure 1.16 Observing continuous displacements with DInSAR (Modified after Cepsa et al., 2016).

The same technique (DInSAR) can be utilized to estimate ground displacement due to subsurface CO_2 injection, where the injection period will be long and the displacement velocities will be rather small and expected the uplift extended over many square kilometres. The most prominent example of InSAR being applied to monitor surface deformation caused by CO_2 storage is In Salah field in Algeria (Figure 1.17).

The In Salah CO_2 storage is a pioneering Carbon Capture and Storage (CCS) project at Krechba, In Salah, central Algeria (Bohloli et al., 2018). More than 3.8 million tonnes of CO_2 have been stored underground between 2004 and 2011. Carbon dioxide is separated from the natural gas and is re-injected back into a deep saline carboniferous sandstone formation down-dip of the gas producing horizon. The CO_2 was injected in supercritical phase through three wells (KB501, KB502 and KB503), and remained in the same phase in the storage. The storage reservoir consists of a 20 m thick Carboniferous, quartz arenite sandstone with average porosity and permeability of 15% and 10 mD, respectively. The sandstone is well-cemented and brittle, contained by tight sandstone and siltstone at the top and by interbedded mudstone, siltstone and sandstones at the bottom. The injection operation has been monitored by various technologies, including 4D seismic, downhole gauge,

interferometric synthetic aperture radar (InSAR) etc. Particularly, the InSAR data provided a unique opportunity to increase our understanding of the coupled hydro-geomechanical factors in the reservoir and associated geological structures such as faults and fractures.

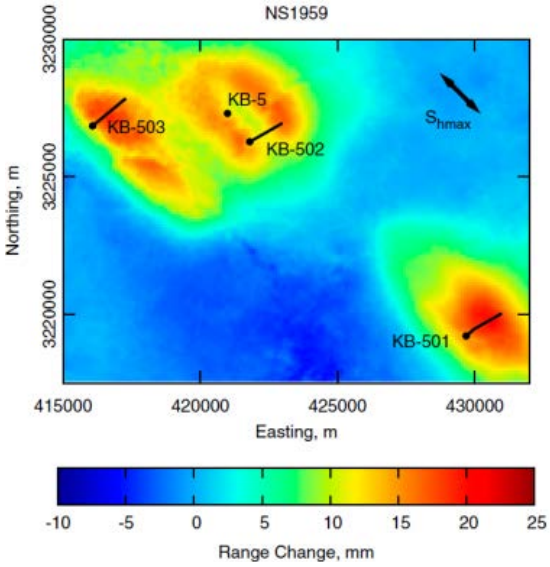

Figure 1.17 InSAR measured surface deformations at In Salah, as of March 2010 (after White et al., 2014).

1.5 Hatfield Moors, natural gas storage-onshore UK

The Hatfield Moor gas storage facility is used in this study as an analogy for an active, onshore CO_2 storage site. The intention is to investigate the use of satellite Interferometric Synthetic Aperture Radar (InSAR) to characterise the volume and location of injected/removed gas via changes in the surface elevation. Although gas is stored at Hatfield Moors at a lesser depth than is typical for CO_2 storage, the site is being used as an analogy for the impacts of fluid injection on a porous reservoir. This enables us to improve our understanding of the link between surface movement and CO_2 injection.

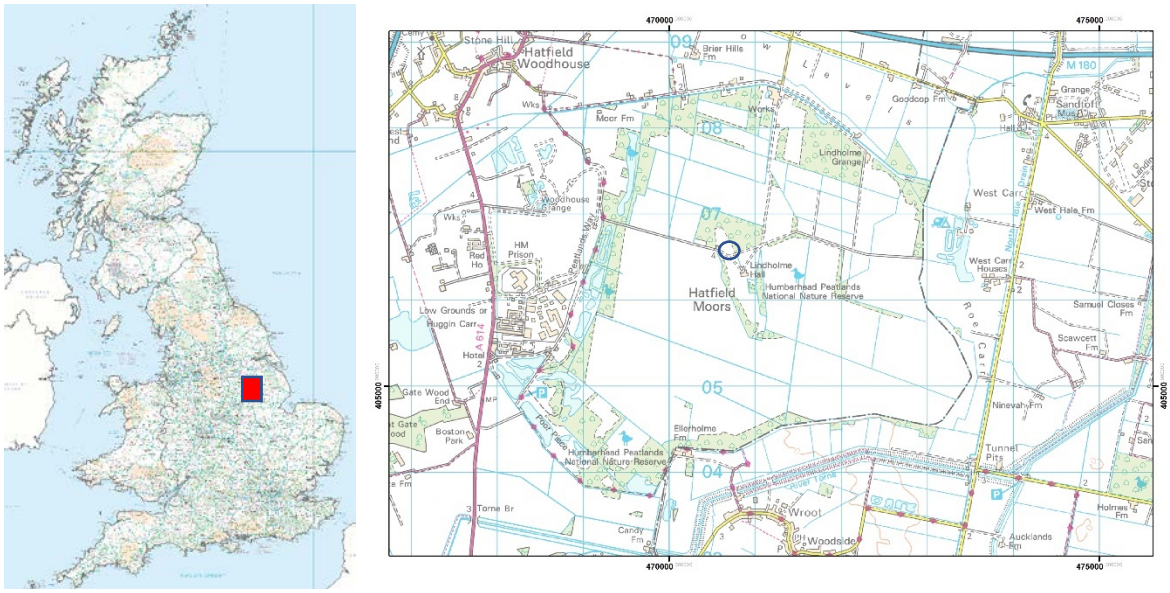

Figure 1.18 Location of Hatfield Moors study site; Scottish Power gas injection site circled in blue. Contains Ordnance Data © Crown Copyright and database rights [2021]. Ordnance Survey Licence no. 100021290.

Study site Geological Setting and characteristics

Hatfield Moors is an ~29 km^2 peatland located in South Yorkshire to the east of Doncaster (Figure 1.18). It is currently part of the Humberhead Peatlands National Nature Reserve managed by Natural England (https://www.humberheadpeatlands.org.uk/). The Moors represent a remnant of a larger wetland which was known as the Humberhead levels, although now much smaller in size they are still the largest area of raised peat bog in the United Kingdom (Mitchell et al., 2020).

Peat was worked from Hatfield Moors from the thirteenth century through to 2001 (with stockpiles used until 2005), although the most was extracted during the 1980's by a technique known as peat milling. Since 2005 efforts have been in place to return the area to a condition under which peat can be formed.

The outcropping bedrock geology of the Hatfield Moors site is the Triassic sandstone of the Chester Formation (Figure 1.19). However, this is overlain by superficial deposits consisting predominantly of Peat, with river terrace sands and gravels to the east, an 'island' of Glaciofluvial clays, sands and gravels and Alluvium to the west (Figure 1.20).

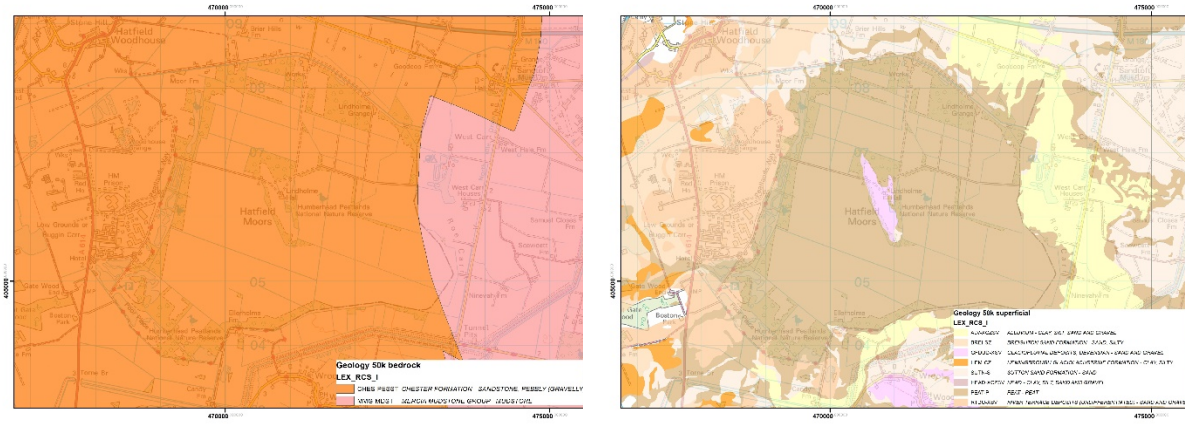

Figure 1.19 Bedrock geology map for the study area (left). Superficial geology map for the study area (right). Contains British Geological Survey materials ©UKRI 2021. Contains Ordnance Data © Crown Copyright and database rights [2021]. Ordnance Survey Licence no. 100021290.

According to the CORINE land cover map (CORINE 2018; Figure 1.18), landcover within Hatfield Moors is dominated by peat bogs (~55%), non-irrigated arable land (~17%), water bodies (6%) and inland marshes (4%). Such types of terrains commonly undergo seasonal variations related to decomposition processes and weather conditions.

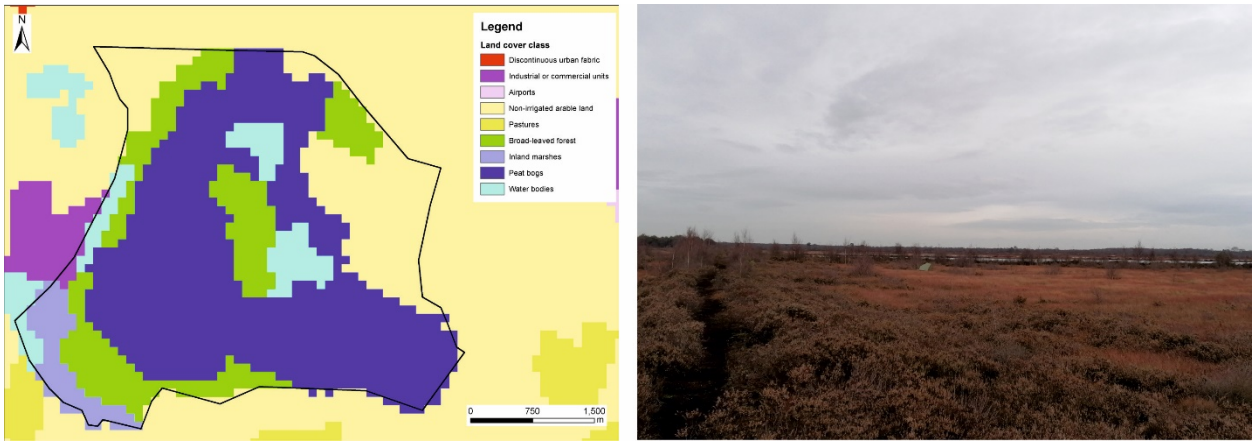

Figure 1.20. Land cover map for Hatfield Moors with the peatlands edge shown with a solid black line (left). Appearance of the peat bogs on site (right).

Gas Storage

The Hatfield Moor gas storage facility utilises a depleted gas field at a depth of approximately 440 metres to store natural gas enabling Scottish Power to manage demand and store gas for peak periods (Scottish Power, 2014; Figure 1.21). Gas is stored in the porous Oaks Rock Sandstone and sealed by a marine bed. The reservoir has a capacity of 116 million cubic metres and has been operational since 2000 (Scottish Power, 2014).

Gas is injected using wells located within the Scottish Gas compound to the west of Lindhome Hall (see Figure 1.18). Gas is stored within the reservoir as outlined in Figure 1.19.

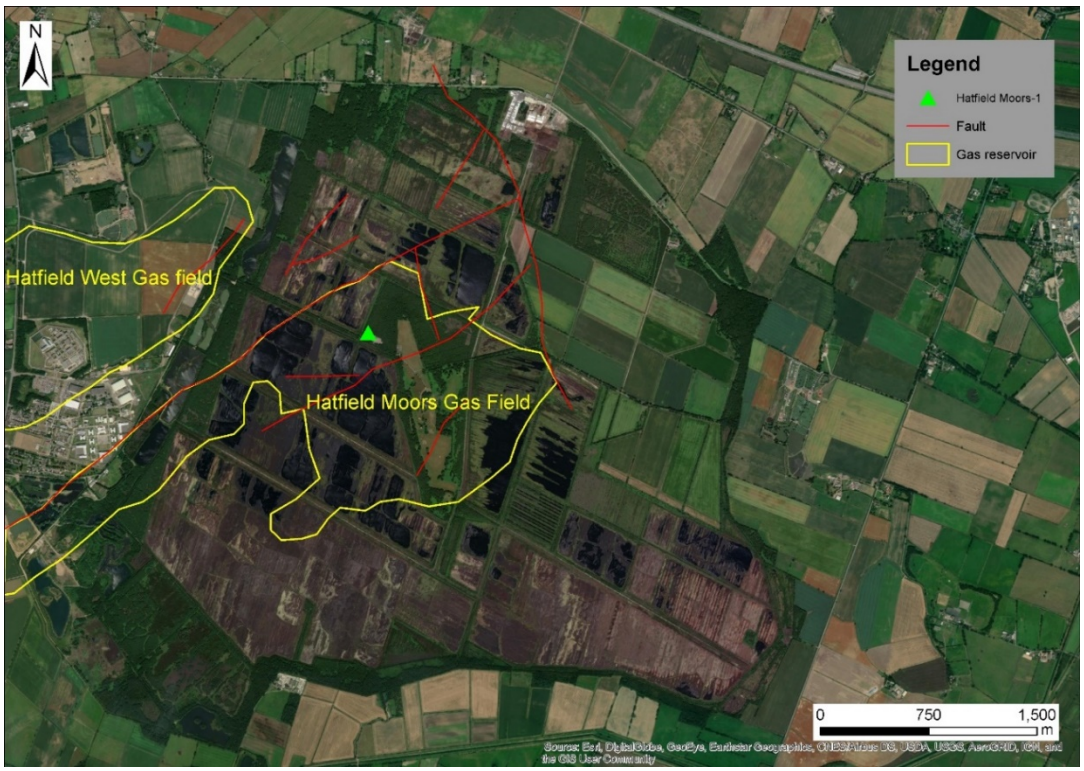

Figure 1.21 Location of gas storage reservoir, faults and injection well under Hatfield moors. Source of the background image: Esri - World Imagery basemap.

The subsurface of the area around the Hatfield West and Hatfield Moors gas fields has been characterised by the interpretation of geophysical data consisting of seismic and boreholes (Figure 1.22).

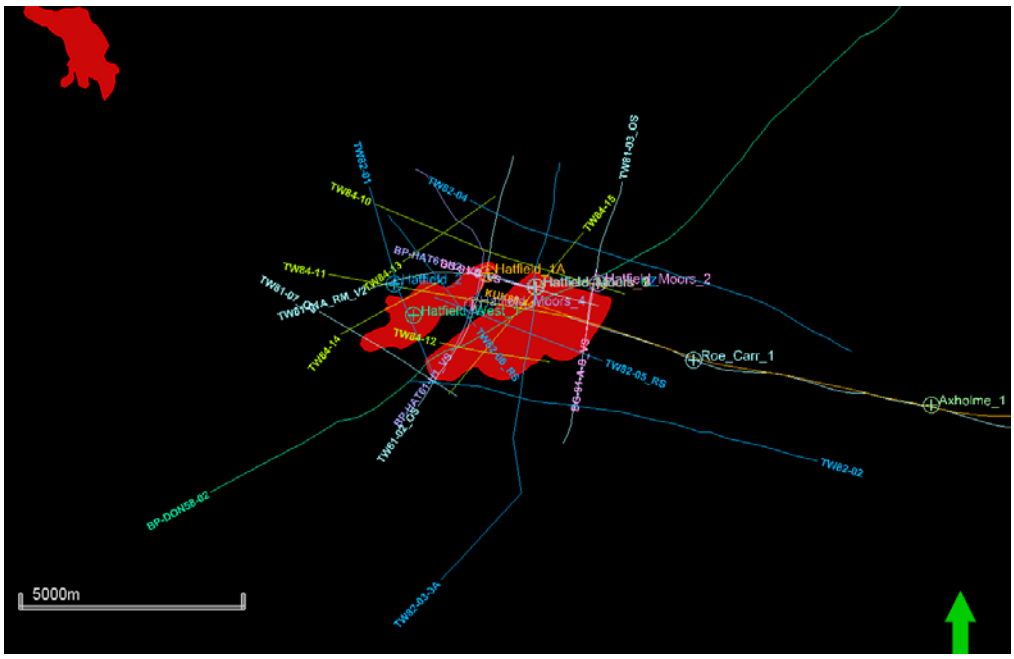

Figure 1.22 Map showing seismic and borehole data used to interpret the Hatfield gas fields.

In the 1960s, BP and others extended the search for hydrocarbons in the East Midlands of England to areas north and west of the Gainsborough and Beckingham Fields in the Gainsborough Trough. Hatfield-1 and Hatfield-2, drilled by BP and the Gas Council in 1966 on a structure east of Doncaster, were unsuccessful. Testing at Hatfield-1 by the Gas Council, however, showed excellent reservoir potential for future gas storage within the shallow Oaks Rock sandstone. In the 1980s, Taylor Woodrow, at the time operator of the Hatfield area, spudded Hatfield Moors-1 at a near crestal location on a close, but separate structure east of Hatfield-1. Four more wells were drilled on the Hatfield structure. Hatfield Moors-5 well is the first UK onshore well designed for gas injection and production from a partially-depleted gas-bearing sandstone.

The UK case study proved challenging owing to the small volumes of gas involved and the nature of the ground cover. The quality of the InSAR data was improved by the placement of corner reflectors, which provided strong reflection points for the satellite data since the ground is vegetated and therefore offers poor repeatability since the vegetation changes with the seasons. The superficial geological cover mainly comprises peat which has a seasonal ground movement signal as it swells in the winter when wet and contracts in the summer when dry. The relatively small volumes of gas being injected and withdrawn from the reservoir meant that the predicted ground movement resulting from gas injection and withdrawal was on the millimetre scale, which is within the noise level for InSAR data.

Processing multiple InSAR data packages provided confidence in the pattern of observed ground movement. Comparison of the results of flow and geomechanical modelling of the Hatfield Moors

site with the interpreted InSAR data indicated a good match between model outcomes and observed data.

In order to extrapolate only relevant information from the large InSAR timeseries dataset, a machine learning technique that clusters datapoints was applied and then used as an input to the BGS 'classifier' automated processing technique (Hussain et al., 2021). This automatic classifier works as expected and helps filter the data, enabling focus on points of interest to confirm interpretation. The effects of the 2018 drought on the peat are clearly observable in the classified InSAR results, suggesting the classifier can be used to pick out signals of interest.

The BGS InSAR 'detector' technique is under development. This technique applies a statistical approach to rapidly assess when new points in the time series are 'significantly' different to the expected trend. Coupled with regular acquisitions (e.g., the European Space Agency's Sentinel-1 satellite constellation), opportunities for near-real time deformation monitoring can be explored. Additional work is needed to refine application of this technique.

Key learnings from this study show that flow and geomechanical modelling have a key role to play in understanding fluid (gas/CO_2) storage site behaviour and demonstrate the value of history matching to provide confidence in predicting site behaviour. These modelling results could be used to consider how much ground movement would be expected at any particular site, and, therefore the role for ground motion detection in the monitoring programme. Practical learnings on collecting baseline data and installing additional equipment on the site ahead of fluid injection to aid in detection of small ground movement using InSAR data were also obtained during this study.

1.6 Hontomín CO_2 storage test site, Spain

The onshore Hontomín pilot plant was developed in 2011 to test the feasibility of geological CO_2 storage in a structural dome formed by salt tectonics in the southern edge of the Basque-Cantabrian Basin (North of Spain) as defined by Ramos et al. (2022), see Figure 1.23. This site has been a case study location in the SENSE project for making the most of either available or accessible data of a real onshore CO_2 storage development. This involved investigating co-injection seismicity during the characterization of the reservoir in 2014, and for the study of post-injection deformation via InSAR technology. The reservoir of this storage complex is a saline aquifer that extends from 900 m depth at the apex of the dome to 1832 m deep in the flanks, within the fractured carbonates of the Sopeña Formation (Lower Jurassic). The basal seal for this reservoir is the evaporitic Keuper (Triassic), while it is confined upwards by a marly Liassic cap-rock (Lower Jurassic). The geology of the site and region is depicted in Figure 1.23 and Figure 1.24.

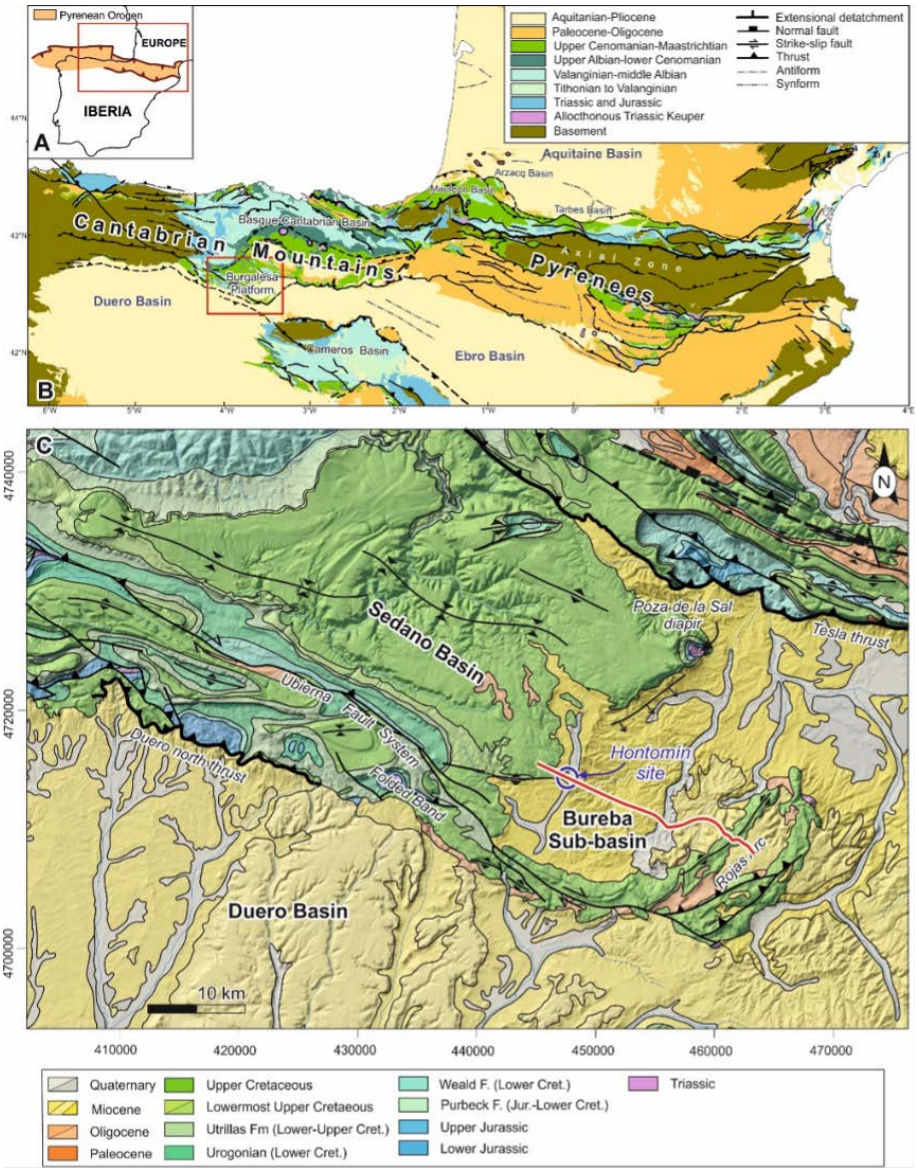

Figure 1.23 a) Inset map of the Iberian and the Pyrenean Orogen. b) Geological map of the Pyrenees and the Cantabrian Mountains. c) Geological map of the Burgalesa Platform and the surrounding Cenozoic basins, showing the main structural elements. The red line shows the cross-section in Figure 1.24. Modified from Ramos et al. (2022).

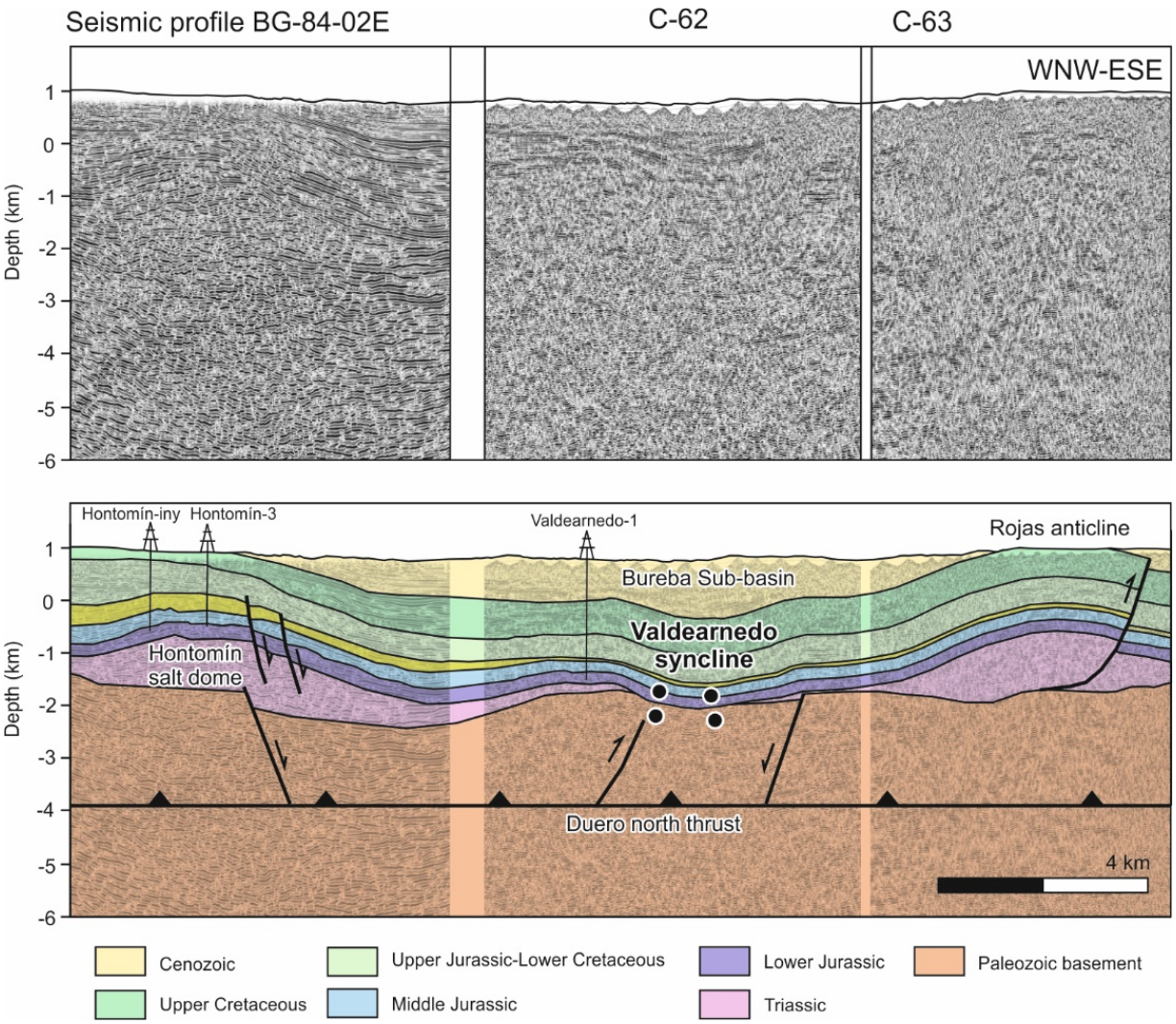

Figure 1.24 WNW-ESE cross-section showing the structure and stratigraphy of the Hontomín study area down to 6 km depth (Ramos et al., 2022). The geological interpretation overlays a 2D seismic profile. The Hontomín salt dome and the location of the injection well (Hontomín-iny) are shown on the left side of the profile. See Figure 1.23 for location.

Fluid injection

Two wells were drilled at the Hontomín Pilot site, consisting of an injection well (Figure 1.25) and an observation well. Both wells reach the basal storage seal, the Keuper Formation. The total amount of fluids injected into the Hontomín storage complex during the characterization phase has been around 2300 tons of CO_2 and 14,000 m^3 of brine that were used to hydraulically characterize the reservoir in 2014 and 2015 (de Dios et al., 2017). The Hontomín pilot plant is the first and only test centre for underground CO_2 storage in Spain and has been considered a key test facility by the European Parliament. CIUDEN constructed all the facilities required for onshore injection and geological storage of CO_2 at Hontomín, with the perspective of being part of a full-chain CCS experimental project.

Data and periods of study

CIUDEN possesses seismicity data for the Hontomín pilot plant from 2010 until the present day. These data are acquired using a surface network of 30 seismic stations positioned radially around the

location of the injection well, covering an area of approximately 8 x 9 km^2 (Figure 1.25). Data are recorded at a 200 Hz sampling rate from two different models of seismic sensors, 10 Lennartz LE-3D/20s and 20 SARA SS-45. Additionally, IGME has collected fault data around the Hontomín site in two different field campaigns and has looked for InSAR data that could be purchased and of use to this project.

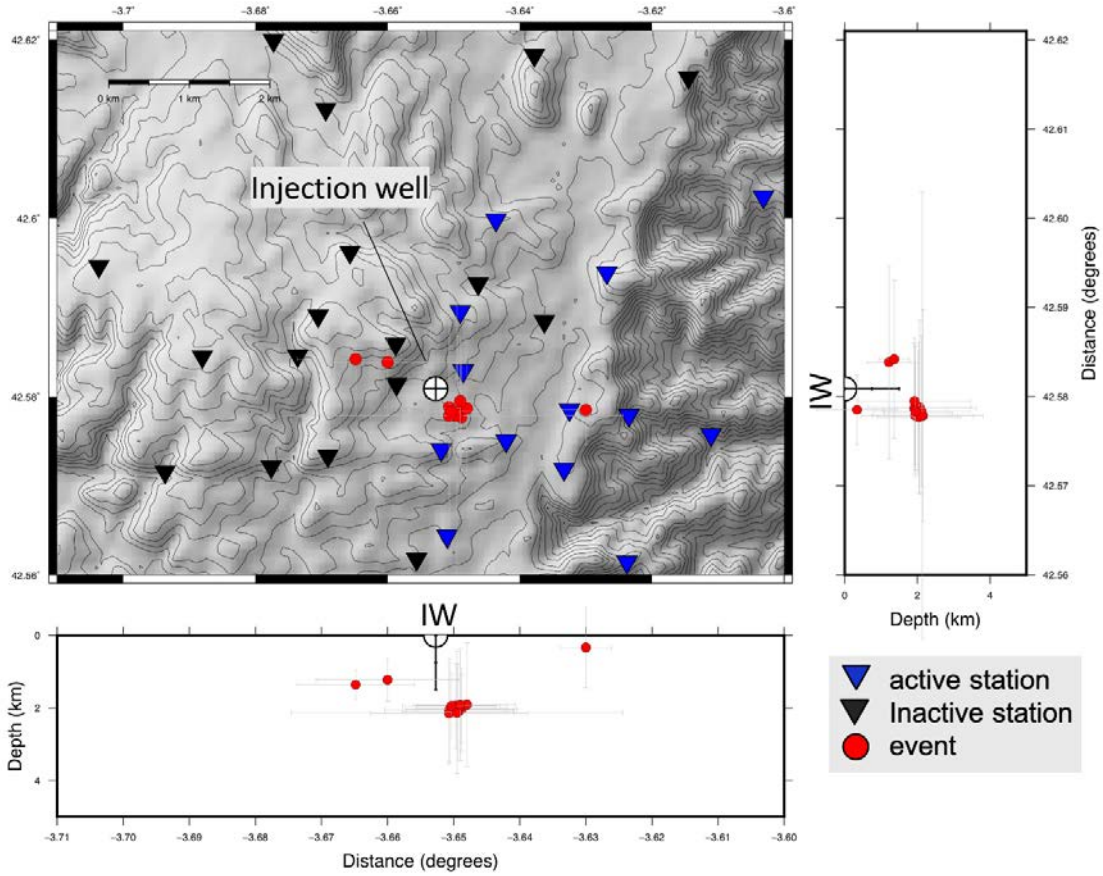

Figure 1.25 Location of seismicity monitoring stations around the Hontomín injection well. The inverted triangles show the location of seismic stations and the white crossed circle represents the injection well. Seismicity hypocenters (red dots) map and E-W, N-S cross-sections.

Once the Hontomín reservoir was fully characterized, a pressure drop valve was assembled in the injection tubing to control bottom hole pressure (BHP) and avoid induced seismicity by the injection. But from May 2014 to December 2015, several sequences of injection tests were carried out prior to that installation, meaning this period was the most prone to induce seismicity. The tests performed in 2014 and 2015 combined different operational modes regarding fluid composition (brine only, brine and CO_2, and CO_2 only), control parameter (pressure control mode versus flow rate control mode) and test duration (short pulses of 7 injecting hours versus continuous injection for 24-72 hours). Based on the temporal variation of BHP and seismicity network performance (Figure 1.26) and the automatic detections of the network, July and September 2014 were selected as the periods of highest interest to this study. With this in mind, seismicity was thoroughly inspected for those periods but unfortunately, there was no Sentinel-1 data for those periods. The Sentinel-1 (S-1) mission from the European Space Agency (ESA) comprises a constellation of two polar-orbiting satellites that were launched in 2014 (Sentinel-1A) and 2016 (Sentinel-1B). For this reason, IGME decided to obtain and work on InSAR images of the post-injection period (2015-2021).

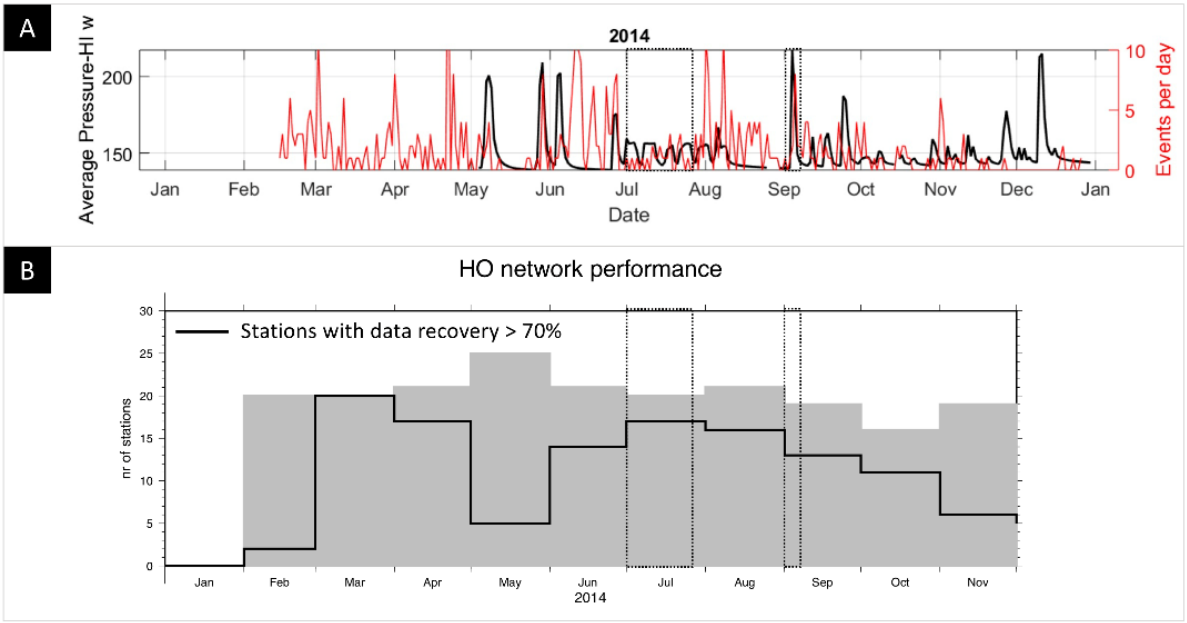

Figure 1.26 Bottom hole pressure (BHP) at injection well, network automatic triggers and network performance in 2014. A) The black line shows the BHP (barg) and the red line shows number of automatic triggers done by the network as provided by the ENOS project in 2019. B) Network performance variations. Grey bars show the number of stations active per month and the black line highlights the number of active stations that recorded at least 70% of the data volume expected. Study periods are marked with black dotted contours.

The IGME team committed to study and estimate the ground movement around the pilot-plant Hontomín geological CO_2 storage, by interpreting the processed InSAR (satellite Sentinel-1 SAR data) data after the injection operations that took place during 2014. In order to achieve this goal, the team carried out two different processing algorithms: 1) P-SBAS stands for Parallel Small BAseline Subset and it is a DInSAR processing chain for the generation of Earth deformation time series and mean velocity maps; 2) FASTVEL algorithm, developed by TRE-Altamira for generating differential interferograms or PSI-based mean displacement velocity maps from a set of Sentinel-1 or ASAR images (Figure 1.27).

The P-SBAS algorithm was performed using 89 and 90 Sentinel-1 SAR images in ascending and descending orbit, respectively covering the period January 2018 to January 2021 (Table 1.1) with no remarkable ground surface movements observed. The FASTVEL algorithm was also performed using 90 Sentinel-1 SAR images in descending orbit, covering the period from November 2015 to November 2017. The threshold coherences used were greater than 0.85 and 0.5, respectively. The processing parameters that can be chosen by the user of both algorithms are limited. As part of Copernicus, that is the European Union's Earth Observation Programme, the Sentinel-1 mission adopted a free, full, and open data policy to all users of the S-1 data products via Copernicus Open Access Hub (https://scihub.copernicus.eu/). We have used the images from this open and free policy.

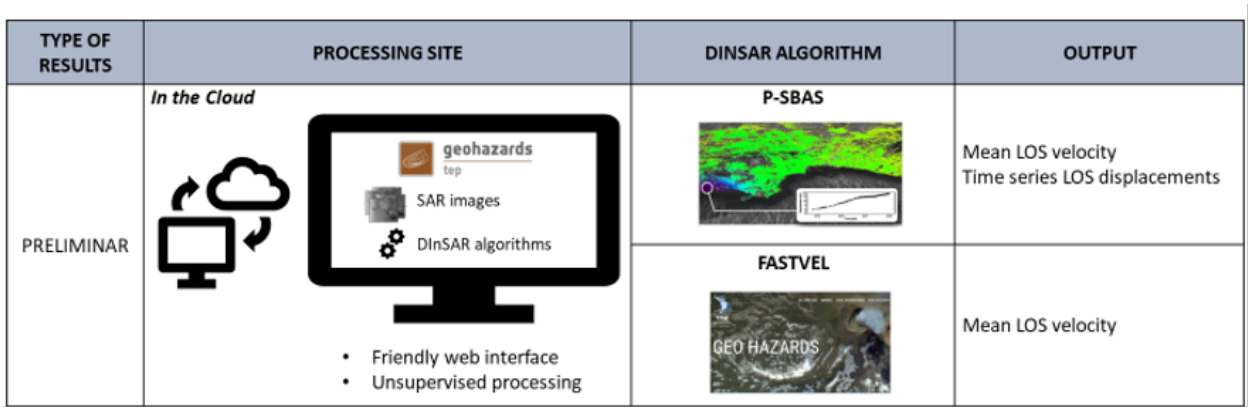

Figure 1.27 InSAR processing steps taken by IGME.

Table 1.1 InSAR datasets processed by IGME.

	P-SBAS A	P-SBAS D	FASTVEL
Number of images	89	90	90
Initial date	05/01/2018	16/01/2018	16/11/2015
Final date	01/01/2021	24/01/2021	17/11/2017
Acquisition mode	Wide Swath (IW)		
Polarization	VV		
Orbit	Ascending	Descending	Descending
Track	1	154	154
Incidence angle of the area processed [°]	36.47° - 41.85°	30.86° - 36.59°	33.73° - 36.59°

CIUDEN and IGME have collaborated in the analysis of deformation data for the Hontomín geological storage test site. The research teams at CIUDEN and IGME agreed to jointly study the effect that injection tests performed in 2014 had on the storage complex, at depth and in the surface. To do so, CIUDEN committed to re-process seismicity data for the period of interest. The aim of this part was to better understand the correlation of seismic events occurrence with the evolution of injection conditions, shedding light on induced deformation in the subsurface around the injection well. This was to be complemented by the analysis of surface deformation led by IGME. IGME focused on the combination of estimating surface uplift and subsidence from InSAR images and detailed structural mapping at high-interest locations, to identify any indications of recent ground deformation or fault reactivation. The determination of the present stress field was considered with the purpose of; a) preventing fault reactivation and related earthquake triggering due to injection processes and the active natural tectonic field; b) minimizing the potential consequences of reservoir leakage and seepage, and therefore preserving the integrity of the reservoir; and c) monitoring the long-term reservoir behaviour. https://scihub.copernicus.eu/.

Results and interpretation

The processing applied to the seismicity data resulted in a catalogue of 16 local microearthquakes that took place in association with injection tests and within the network area. Local magnitudes range from -1 to 0.4 (ML) and microseismic sources locate very close to the injection well bottom (Figure 1.28), which would correlate with very small rupture areas in the reservoir, thus unlikely extending to the surface or compromising the seal. There is a notable scatter in the temporal distribution of seismicity (Figure 1.29), with only three sparse microearthquakes accompanying the injection tests of July 2014 and thirteen microevents clustered around the longest injection test of the summer 2014, at the beginning of September. This shows a correlation between seismicity occurrence and BHP, as the microseismicity cluster of September is related to the highest BHP reached during that summer.

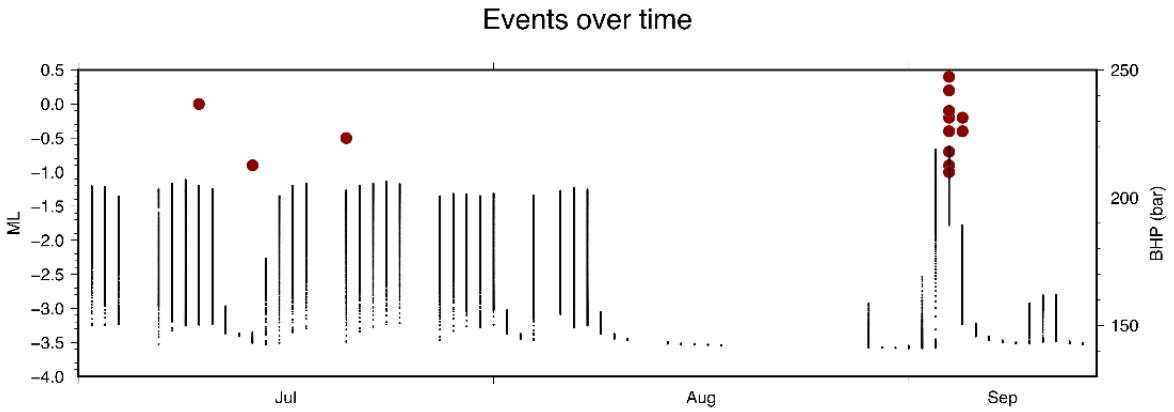

Figure 1.28 Seismicity occurrence (red dots) and bottom hole pressure at injection well (fine black dots) during July-September 2014 at Hontomín.

Although it is difficult for microearthquakes, it was possible to determine the focal mechanism for three of the events in the cluster that occurred in September and invert these to obtain local stress fields. The focal mechanism solutions all show hybrid kinematics with a strong strike-slip component and a minor reverse component (Figure 1.30). The similarity in mechanisms might represent a common source structure for the three events or a geological structure configuration that is preferential for slipping/failing in the context of the Hontomín plant area. The results for the local stress field are also similar and show a maximum horizontal stress orientation that varies between East and Northeast (Figure 1.29), which is a very useful input to perform any seismicity or deformation modelling and/or plan future injection activities.

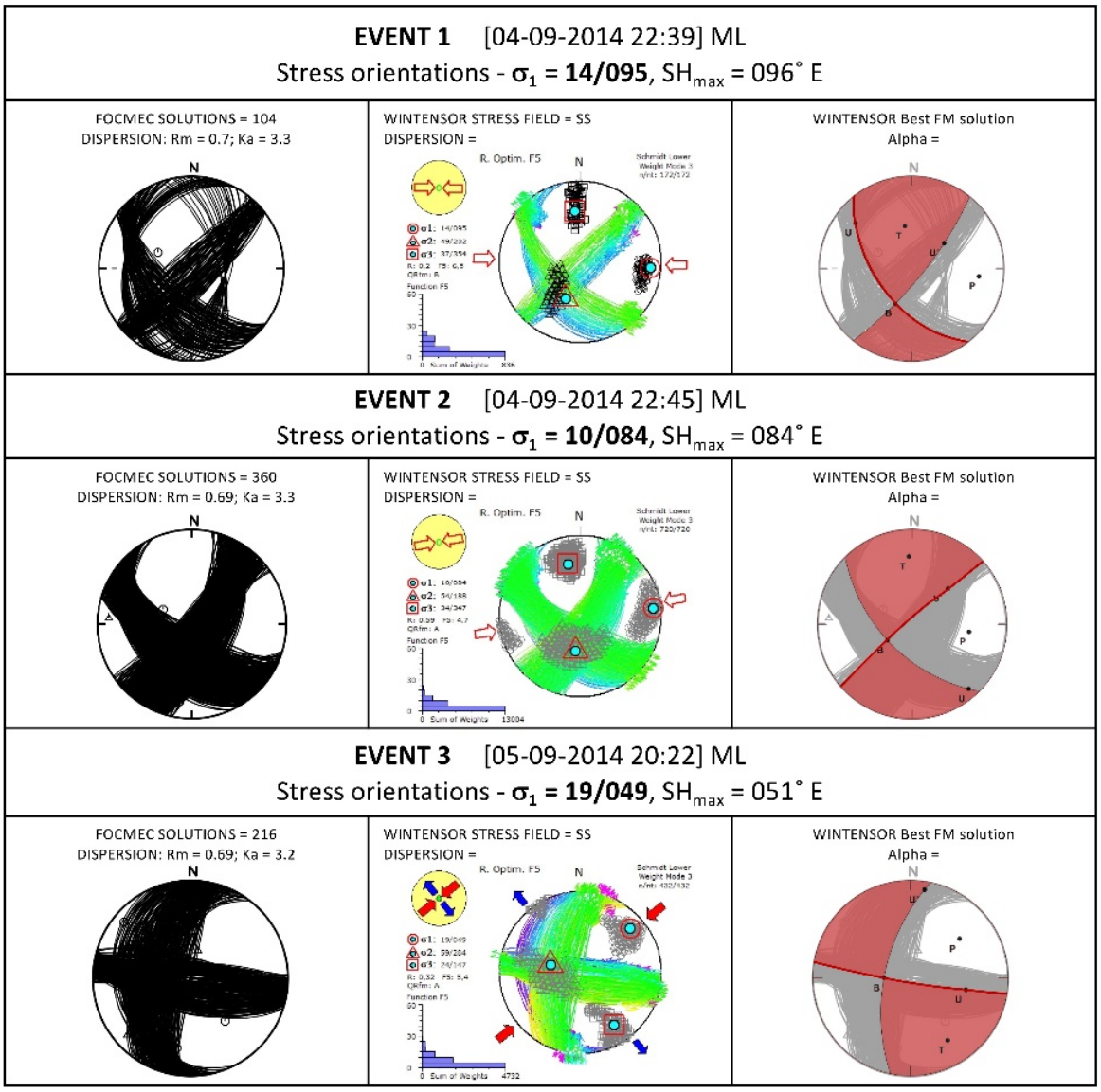

Figure 1.29 Focal mechanism and stress field results. The graphics on the left show all focal mechanism solutions for each event, for which the best solution is colored in red on the graphics on the right and the stress field results are shown in the central figures.

No remarkable ground surface movements can be determined from the P-SBAS and FASTVEL processing maps after velocity ranks are adjusted using the standard deviation of data (Figure 1.29). However, when adapting velocity ranks adjusted to only 1 standard deviation of data, it is possible to observe red areas with velocities ranging from -0.5 to -1.5 cm/year and -0.5 to -1.6 cm/year for ascending and descending P-SBAS respectively (Figure 1.30). Some of these areas represent known rapid ground movement, such as the one located west of the Hontomín site, which corresponds to an active gravel pit (Figure 1.30). We cannot rule out uplift nor subsidence with a magnitude lower than that observable on the InSAR images used; however, due to the small volumes of fluids injected at Hontomín, these might not have induced any surface deformation.

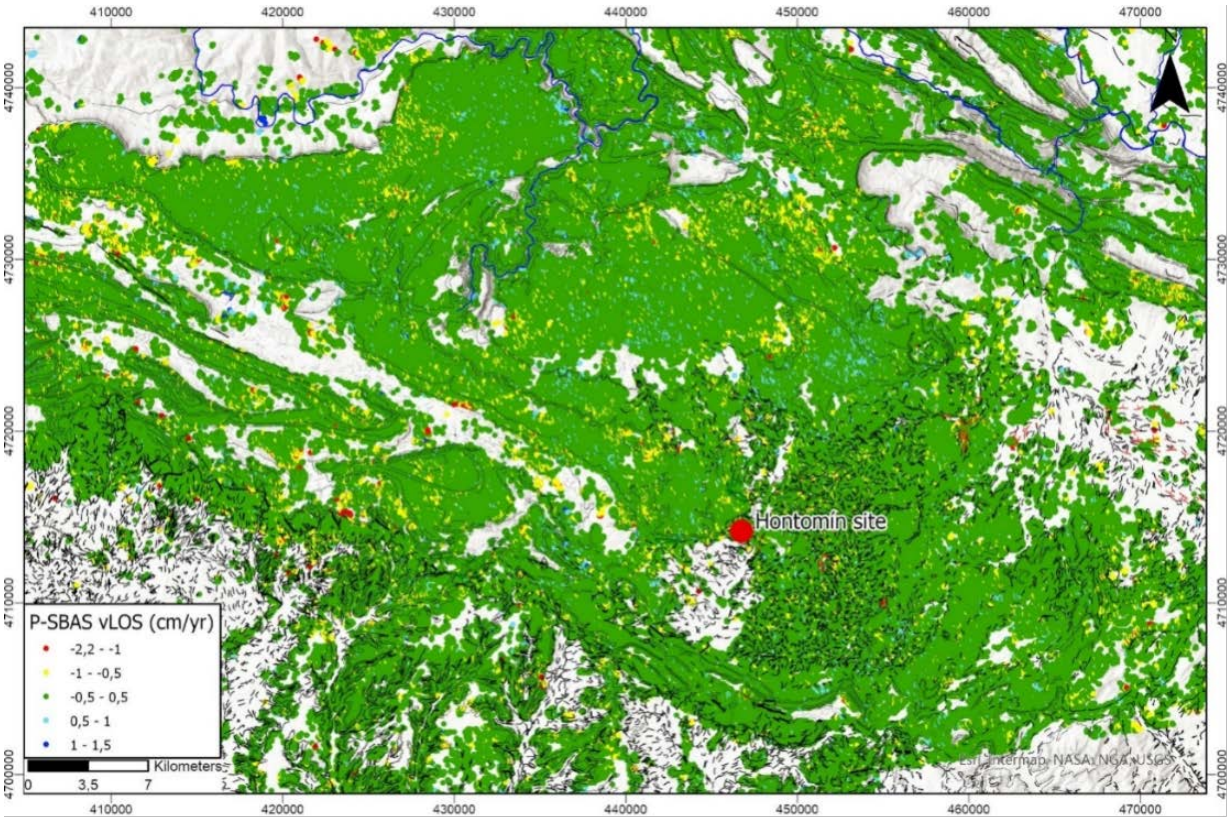

Figure 1.30 LOS velocity of the full extent processed with P-SBAS Ascending. Period January 2018 to January 2021.

Conclusions and lessons learned

The injection tests performed at the beginning of July and September 2014, at Hontomín, were accompanied by seismicity in the 'micro' seismic magnitude range, which is highly common and expected for underground fluid injection activities and no induced seismicity has been observed. There is a correlation observed between microseismicity occurrence and the bottom hole pressure (BHP) at the injection well. Thus, installing a control system for BHP, as it was done at Hontomín, can be a powerful seismicity mitigation procedure. This case study has served as a test for the ability of surface seismic networks to detect microseismicity which can help reduce monitoring costs, through a convenient surface deployment design. Moreover, the automatic monitoring system implemented with the Hontomín network detected only scarce local seismicity for the period under study. Thanks to the new inspection of the data investigated, an increase of 90% detected events were reached and this is a very useful input to adjust the settings of the automatic seismicity detector, so that it triggers as many of the induced events as possible.

No surface deformation was identified on InSAR data for the post-injection period (2015-2021) at the Hontomín site. This might be because no deformation was caused by the injection tests or because deformation at the surface was so small that it cannot be observed on the InSAR data used. New and more efficient seismicity data processing software is being developed, involving Artificial Intelligence (AI). Through this work, we have explored new tools available and we found there are interesting alternatives to process seismicity data, such as integrated processing platforms (i.e.: LAKIY, developed by the Servicio Geológico Colombiano; EZW Earthworm platform by ISTI; SMARTMONITORING software platform by QUAKELOGIC). These platforms offer a package of

connected tools that provide near real time seismicity catalogues that can be consulted online or via an App, accelerating decision-making. Although it was not applied nor needed for the Hontomín pilot Plant, we recommend the design and use of a Traffic Light System (TLS) to mitigate potential seismicity effects. Ideally, this protocol would involve a seismicity simulation and be adaptive (ATLS), meaning the model is updated as monitoring data is acquired, so any prediction takes in to account the latest variations in the reservoir. Further, this should be incorporated with any other deformation data into a common multi-data and/or multi-parameter control system.

1.7 Gulf of Mexico case study

The northern Gulf-of-Mexico is a promising offshore resource to permanently store carbon dioxide and mitigate greenhouse gases in the atmosphere. Monitoring techniques, such as 4D seismic surveys, electrical and electromagnetic surveys, gravity measurements, and down-hole pressure measurements have been employed to ensure CO_2 containment in large-scale storage offshore sites (Camargo et al. 2022, De Angelo et al. 2019, Ruiz 2019). While these are well established monitoring techniques, deformation monitoring has been sparsely used in an offshore context (Camargo et al. 2013) given that equipment must withstand more adverse conditions than for onshore sites, and the cost of deployment and maintenance can be substantially higher. Monitoring deformations can be beneficial not only for ensuring reservoir containment but also for ensuring geomechanical stability of the storage complex. The goal of this work is to provide recommendations regarding appropriate deformation monitoring techniques with sufficient deformation sensitivity to obtain valuable data assessing geomechanical responses to CO_2 injection at the High Island 24L leasing block in Texas state waters. While there are no immediate plans to store CO_2 in the HI24L site, the reservoir's lithology and structure are representative of a broad number of potential storage targets in this region. We have used 3D seismic and well data to build a detailed geologic model honoring the stratigraphy and fault structure at the site. Then, we assess the deformation and excess pore pressure resulting from injection using a tightly coupled finite-element/finite-volume simulator to model compositional flow of CO_2 in the brine-saturated deformable porous medium. Finally, the numerical results are analyzed to draw conclusions on an appropriate deformation monitoring technique for the expected geomechanical response.

The High Island 24L study area

The study area is located near the south-east coast of Texas in the Gulf-of-Mexico (Figure 1.31). For management purposes, leasing maps for hydrocarbon production in the Gulf-of-Mexico are divided into blocks, with the High Island 24L (HI24L) block forming a 12 x15 km area approximately 15 km offshore. The High Island region has a considerable potential to permanently store large quantities of carbon dioxide in the Miocene sand strata given that its layers have high porosity and permeability and are separated by transgressive shale intervals that exhibit effective sealing properties (see Camargo et al. 2022 and citations within).

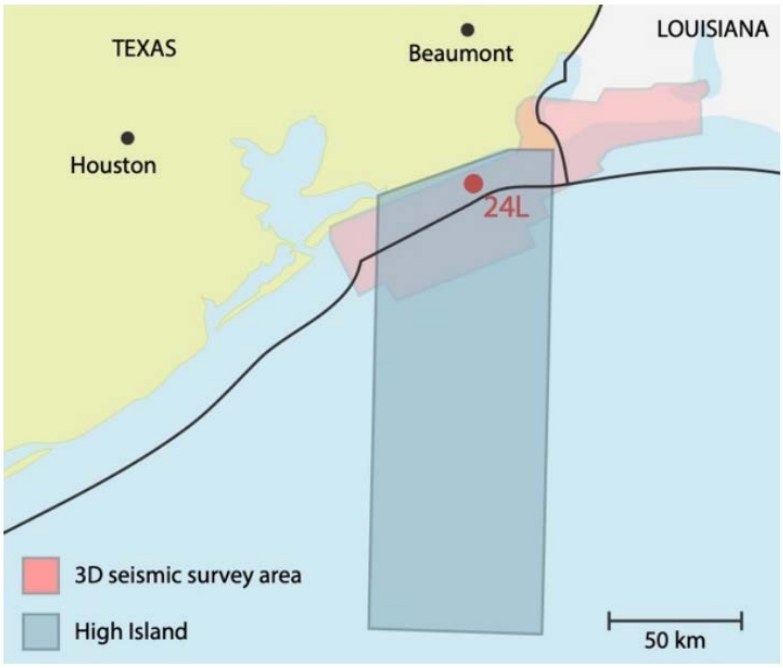

Figure 1.31 High Island 24L location.

2. Geomechanical modelling of CO_2 storage sites with focus on ground deformation

2.1 Geomechanical modelling of In Salah site and synthetic cases

We have carried out numerical simulations of synthetic cases (representative for real storage sites) as well as actual CO_2 injection reservoirs (In Salah). The synthetic cases were simulated for evaluating the observability of surface displacements and for optimizing monitoring plan to tell when, where and for which conditions, surface displacement monitoring can be useful. Three synthetic cases (Carbonate, Sandstone I and Sandstone II cases) were considered that contain different geological features; with and without faults (Figure 2.1). In this study, the injection site is considered as onshore. Thus, surface information is directly available and only monitoring tools for onshore context are studied.

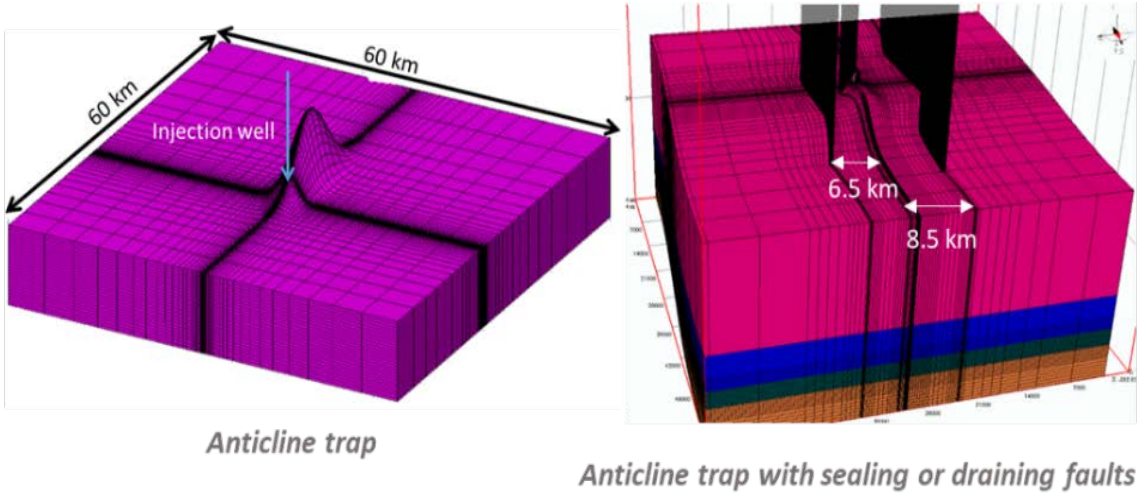

Figure 1.1 Anticline conceptual models. Left: anticline trap without fault; right: anticline trap with two major faults and a sub-seismic fault.

The main hypotheses regarding the CO_2 injection modelling and subsequent surface displacements are listed below (see Bouquet et al., 2022 for further description):

- 3D model 60 km x 60 km
- Open flow boundaries
- 2-phases flow
- Single continuum model
- Homogeneous and static properties
- Poroelasticity only
- Sequential hydromechanical coupling
- No thermal effects are considered
- Drucker-Prager failure criterion is calculated for risk analysis (but we do not model the impact on subsurface/surface when failure criterion is reached).
- Different storage conditions for each scenario, but injection conditions are restricted to a maximum overpressure of 50 bar and a maximum injection rate of 1 Mt/yr.
- Nine parameters are considered as critical and uncertain as defined in Table 2.1

Table 2.1 Uncertain parameters and related ranges of values for the three scenarios.

VARIABLES – UNCERTAIN PARAMETERS	**Carbonates** min-max	**Sandstone I** min-max	**Sandstone II** min-max
Storage Fm Porosity [-]	0.15 – 0.25	0.1 – 0.3	0.1 – 0.2
Storage Fm Permeability [mD]	**15 – 150**	**5 – 50**	**100 - 1000**
Storage Fm Young Modulus [GPa]	**25 – 45**	**2 – 15**	**5 – 20**
Storage Fm Poisson coefficient [-]	0.15 – 0.25	0.2 – 0.3	0.15 – 0.25
Overburden Porosity [-]	0.05 – 0.4	0.05 – 0.15	0.05 – 0.15
Overburden Permeability [mD]	2e-3 – 6e-2	1e-3 – 1e-1	1e-4 – 1e-2
Overburden Entry Capillary Pressure [bar]	5 – 60	10 – 50	5 - 50
Overburden Young Modulus [GPa]	**6 – 55**	**1 – 20**	**30 – 40**
Overburden Poisson coefficient [-]	0.15 – 0.35	0.2 – 0.35	0.2 – 0.3

Based on coupled hydromechanical simulations, the applied methodology evaluates the surface displacements for considered scenario and related uncertainties. The workflow includes uncertainty analysis of the surface displacement observability (statistics of surface displacements) to define where (area) and when (time periods) are measurable with a tiltmeter and InSAR technology, considering their respective accuracy. It also considers sensitivity analysis to define the most sensitive uncertain parameters for which the surface displacement would be the most informative. Recommendations are then drawn for the design of monitoring plan by targeting the most sensitive locations and periods.

Figure 2.2 illustrates results from statistical analysis for InSAR detection capability for each scenario and the subsequent recommended monitoring area in each case. Figure 2.3 shows the expected surface displacements predicted by models according to the uncertainty scenario. When they are discriminating, the surface measurements can be used through model inversion to constrain the values of the coupled model parameters (flow and mechanical) and thus better capture the storage behavior. This can also be used to quickly analyze any a priori abnormal surface behavior and identify structures that might have been missed in the first phase of exploration. Figure 2.4 illustrates the deviations in surface displacements induced by sealing faults with no more symmetrical shape, and the maximum displacements shifted from the well location. This shows the high potential to detect structural irregularities such as faults through asymmetrical, anisotropic areal results with surface monitoring technologies as InSAR monitoring tool.

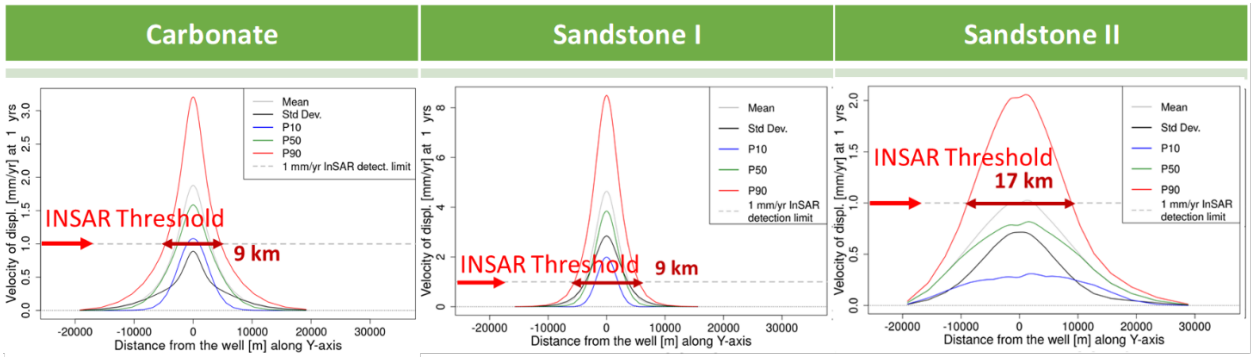

Figure 2.2 Spatial InSAR detection capability (a) for Carbonate case, (b) for Sandstone I case, (c) for Sandstone II case. Cross section along the well - Surface displacement velocities (mean, standard

deviation, median, quantiles 10% and 90%) after one year of CO_2 injection, related to the subsurface uncertainties. Statistical calculations are performed from a Monte-Carlo sampling on metamodels built from the training sample.

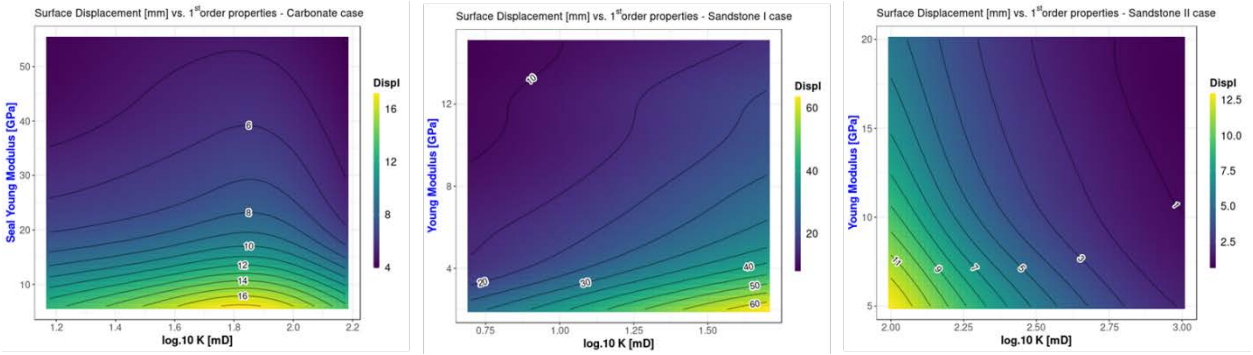

Figure 2.2 Expected maximum surface displacement function of the most sensitive parameters for each scenario.

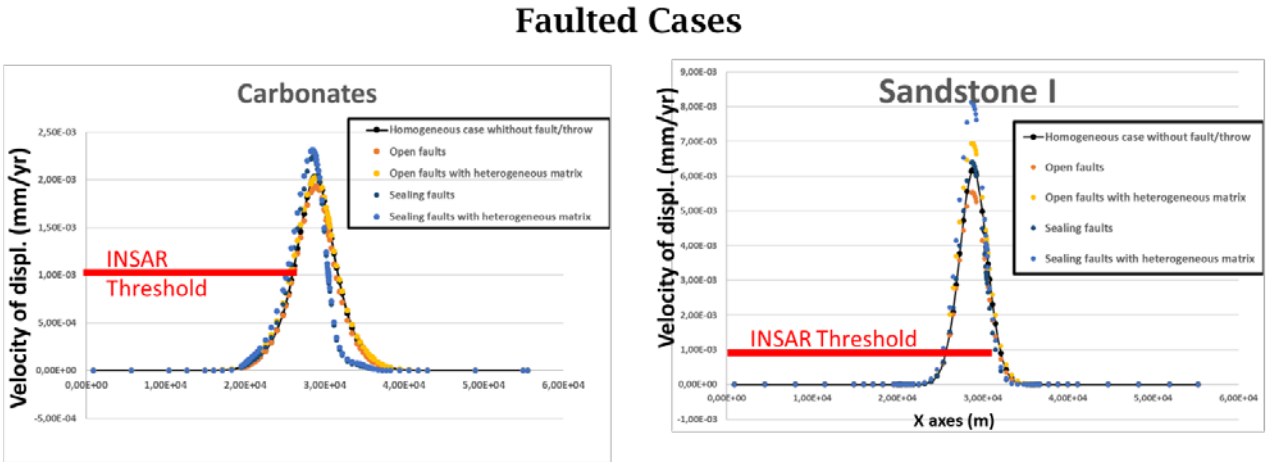

Figure 2.3 Comparison of displacement velocity for structural models with faults after 1 year of injection (a) Scenario Carbonate, (b) scenario Sandstone I.

To optimize the tiltmeters locations, we suggest selecting locations corresponding to a high dependency (Da Veiga, 2015) between tiltmeters measurements and uncertain properties, in addition to the highest variances for tiltmeters measurements based on uncertainty analysis and corresponding simulations. Comparing a posteriori distributions of permeability values based on observations from these locations and on several random locations with pseudo-real observations data as in Figure 2.5, the selected locations data allow to better constrain a posteriori distribution close to the targeted subsurface properties. The use of dependency values, here associated to standard deviation results, could be a quick assessment method (without requiring the resolution of the inverse problem) to estimate informative locations for observations and optimize the monitoring design.

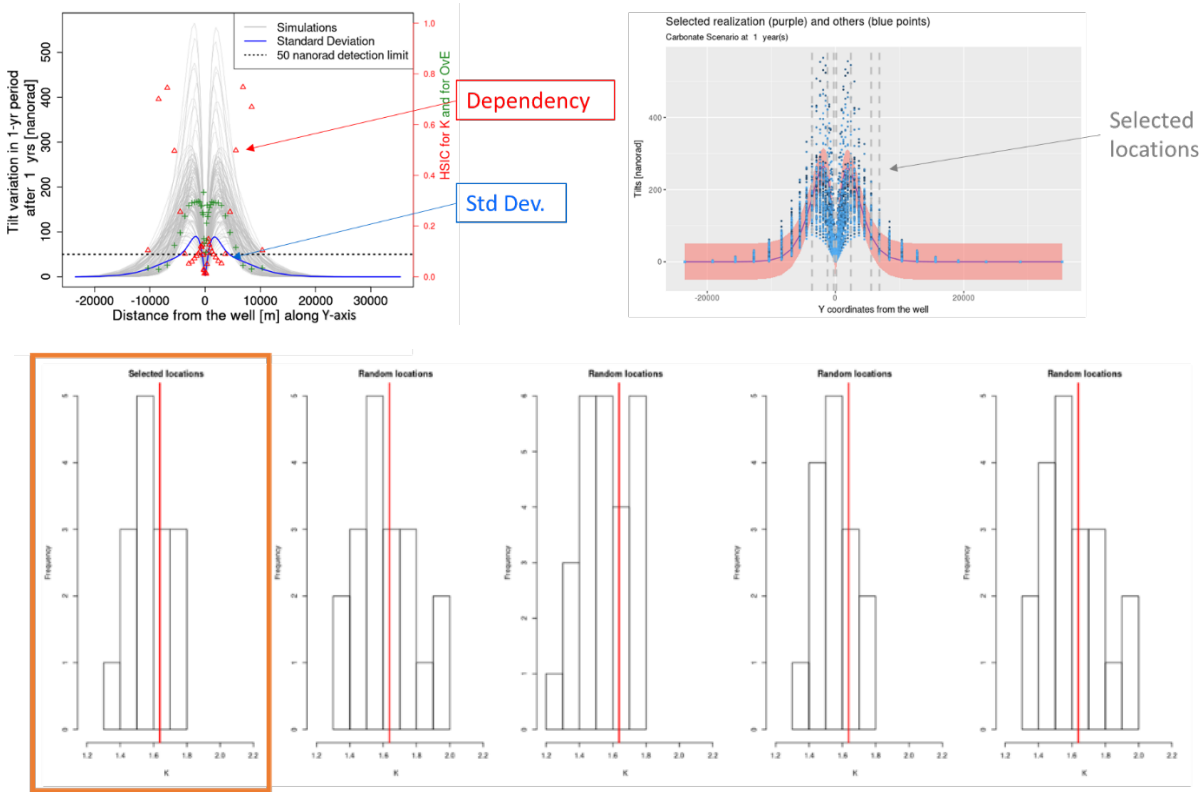

Figure 2.4 Example from the Carbonate Scenario. (a) Tilts simulations results from all simulations (grey lines) and its related standard deviation (blue line) and dependency (HSIC) results between tilts and storage formation permeability (K, red) or caprock Young Modulus (OvE, green) (b) Selected locations (vertical grey dashed lines) based on these results. The purple line is tilts results from a randomly selected pseudo-reality with an observation error of +/- 50 nanorads (pink area). Blue points are tilts results that are obtained from the remaining simulation results. (c) A posteriori distribution estimation for storage formation permeability based on observation data on simulation results at selected location for tiltmeters or at random locations (pseudo-real value to be matched in red). A priori distribution was uniform between 1.2 and 2.2.

Results from the risk analysis are outlined in Table 2.2 for caprock and faults integrity for several stress regimes. This emphasizes the importance of the initial stress regime for the storage integrity and the need of properly define the initial stress regime before considering CO_2 injection. Such an analysis can be carried out to better constrain injection conditions, to identify where and when a storage may be at risk and to localize critical point/areas that need to be accurately monitored such as in Figure 2.6.

Table 2.2 (a) Caprock Integrity analysis results, (b) Fault integrity analysis results for different stress regimes. Green: all stresses are below inner Drucker-Prager criterion (low risks), yellow: some stresses are between inner and outer Drucker-Prager criterion, red: some stresses are beyond outer Drucker-Prager criterion (storage is at risk).

	Carbonate – *caprock*		Sandstone I- *caprock*	Sandstone II - *caprock*
Compressive	18%			
Extensive				
Strike slip	34%	6%	39%	52%

	Carbonate - *Faults*	Sandstone I - *Faults*	Sandstone II - *Faults*
Compressive			
Extensive			
Strike slip			

Carbonate	Sandstone I	Sandstone II

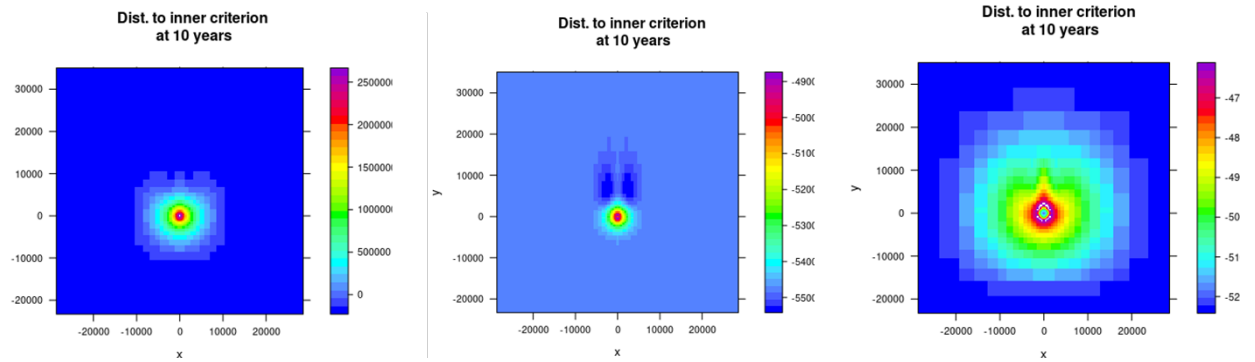

Figure 2.6 XY-cross-sections of distances to failure criteria in caprock (interface storage formation / caprock) in compressive context after 10 years of injection. Coordinates are function of the distance from the well.

Table 2.3 summarizes key results obtained from the developed workflow to help designing the surface displacement monitoring plan:

- Definition of where/when surface displacements are measurable
- Location of measurements to better constrain the sensitive parameters
- Definition of additional locations with a risk analysis based on a failure criterion
- Early warning of unexpected behavior if the monitored surface deformation does not correspond to the expected one (estimated by simulations) and quickly define the actions of remediation
- Recommendations to acquire critical data from the sensitivity and risk analysis

Table 2.3 Summary of key results and recommendations from synthetic cases.

Example Cases	Key Surf. Displacement results [mm]	Recommended monitoring area [InSAR max. resol.]	Required Surf. Displ. Resolution	InSAR value	Tiltmeters value	1st order uncertain properties (sensitivity analysis)
Synthetic Carbonate [Brindisi - Michigan Basin "like"]	Well - P50 - 10 years: 7 mm	9x9 km²	Medium	**High InSAR resol. required** but potential of InSAR technology to detect structural irregularities	Useful	K (storage fm permeability) E_seal (seal Young Modulus)
Synthetic Sandstone I [In Salah - Gorgon "like"]	Well - P50 - 10 years: 17 mm	9x9 km²	Low	**Useful** - High potential of InSAR technology to detect structural irregularities	for early warning in wells area (continuous recording)	K (storage fm permeability) E (storage fm Young Modulus)
Synthetic Sandstone II [Snohvit, Decatur, Otway "like"]	Well - P50 - 10 years: 3 mm	17x17 km²	High	**Low** but if any: potential of InSAR technology to detect structural irregularities	Useful	K (storage fm permeability) E (storage fm Young Modulus)

Finally, compared to data measured locally at the wells, surface data give 2D information of the subsurface behavior with InSAR or continuous records with tiltmeters in informative or risky areas while 2D/3D seismic give the same advantages but at a lower time frequency due to higher costs. The use of the surface deformation as monitoring data help to improve the knowledge on pressure propagation and to monitor CO_2 storage behavior with additional constraints on subsurface properties. In addition, the analysis of the surface deformation shape brings information on the subsurface structure/objects if detectable with a high potential of InSAR data to detect strong heterogeneity and structural irregularity:

- Near well surface displacements: a shift between the location of the center of the maximum surface displacement area and the well might indicate the presence of a strong heterogeneity,

- An evolution of this shift would indicate an evolution of the heterogeneity properties and a possible CO_2 migration through it,
- Post-injection monitoring: a shift after injection may reveal structural influence on plume migration.

2.2 Impact of morphology on ground deformation modeling

A numerical simulation of In Salah was conducted to investigate the impact of reservoir topography on the distribution of initial gas and the plume of injected CO_2. A new static model was developed to represent the reservoir topography accurately and was subsequently rotated by 30 degrees clockwise to align the principal stress direction with its boundary (Figure 2.7). A dual grid system consisting of separate grids for the reservoir flow and geomechanics calculations was implemented using the compositional reservoir simulator, GEM software of the Computer Modeling Group. The exchange of information between the reservoir and geomechanics simulators was accomplished in an iteratively coupled way, resulting in a significant reduction in computational time compared to a single grid coupled simulation.

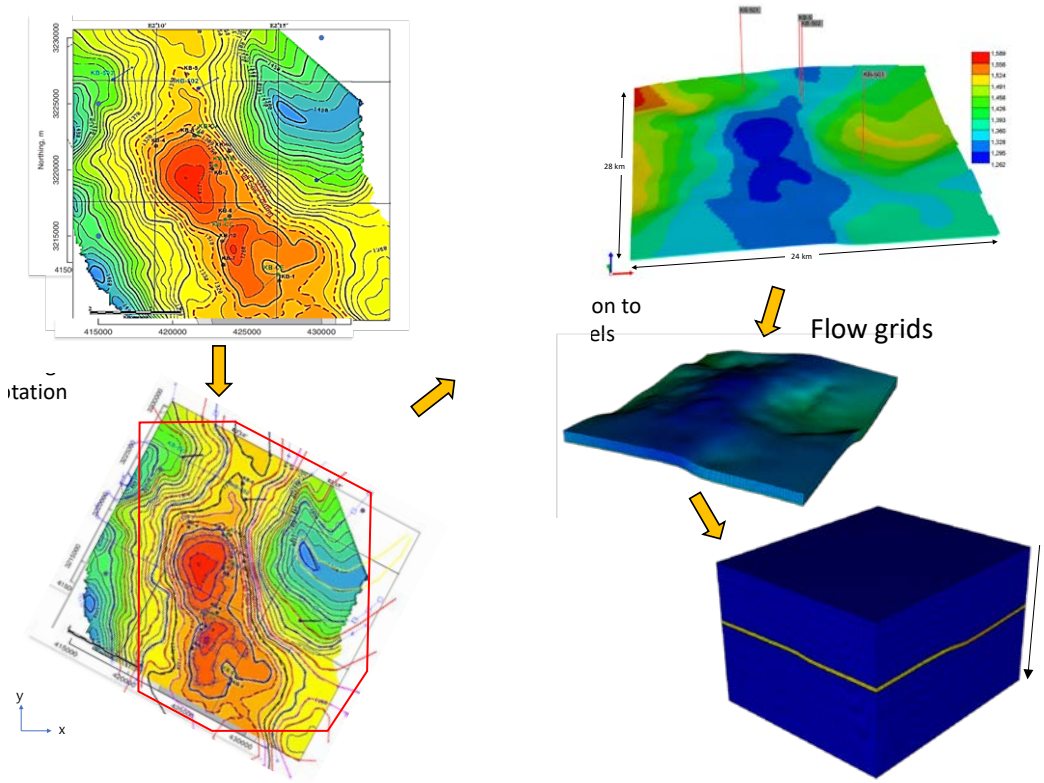

Figure 2.7 A new static model considering the reservoir topography for flow and geomechanics-coupled simulation.

Using the developed static model, reservoir pressure and surface displacement induced by CO_2 injection were computed through dynamic flow and geomechanics-coupled simulation. The results showed that the presence of initial gas (Scenario 2; orange line) in the vicinity of the injection wells brought lower wellhead pressure and less ground uplift compared to the scenario where gas was absent (Scenario 1; black line) (Figure 2.8). This effect was particularly pronounced when the injection well was adjacent to the gas reservoir, with only half of the deformation observed in the

closest well KB502 compared to the simulation result assuming gas absence. The high compressibility of natural gas in the reservoir above the aquifer may have played a role in mitigating the pressure increase. In Scenario 2, where initial gas was considered, lower permeability and Young's modulus were required to match the same level of uplift as observed in the aquifer-only case. In order to describe the double-lobe shape heave occurring around the KB502 injection well, the F12 fault, which intersects the well, was considered. Among several hypotheses, the assumption of a tensile opening of the vertical fault could make the double-lobe shape, achieved by pressure-dependent permeability and much lower horizontal Young's modulus compared to the surrounding formation (Figure 2.9). Additionally, natural gas production was considered in the simulation, which resulted in ground subsidence near the production wells and reduced uplift around the CO_2 injection wells. However, no data were available for gas production, so the effect of natural gas production could not be examined quantitatively. The study highlights the importance of considering reservoir topography and gas production in geomechanical modeling as they significantly impact reservoir pressure and ground deformation.

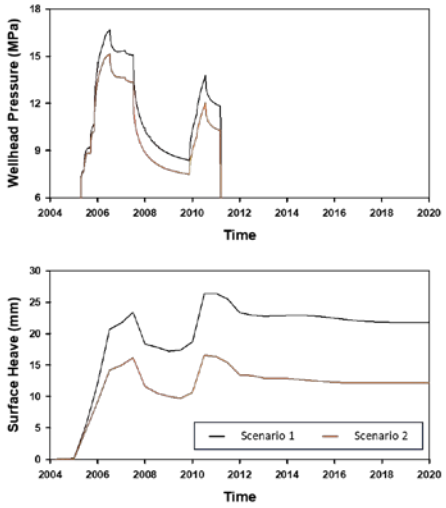

Figure 2.8 The effect of initial gas presence on wellhead pressure and surface heave for the KB502 injection well.

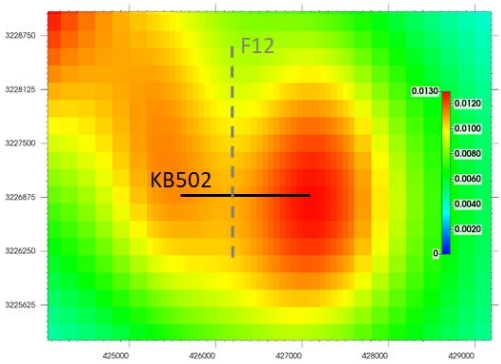

Figure 2.9 The double-lobe shape heaves around the KB502 injection well generated in the coupled simulation.

Synthetic tilt vectors from finite element simulations performed by CSMP coupled geomechanics and hydraulic fracturing simulator (Salimzadeh et al., 2018; Paluszny et al., 2018; Paluszny et al., 2020; Deb et al., 2021) have been used to infer the shape and direction of the CO_2 plume. Details can be found in Salimzadeh et al. (2022). A set of 10 tiltmeters presumably installed on top of the fault near KB502 show that the ground surface deformation initially corresponds to the inflation of the horizontal layer around KB502. Then quickly the ground surface deformation changes to the one corresponding to a vertical plume (pressurization of the vertical fault). The obvious change in tilt vectors occurs when the surface displacement is sub-millimeters, impossible to detect by InSAR technology.

2.3 Geomechanical modelling of Gulf of Mexico

The High Island geologic structure has been mapped by correlating 3D seismic data with spontaneous potential and sonic well logs (DeAngelo et al. 2019, Olariu et al. 2019, Ruiz 2019). Ruiz and colleagues provided a detailed stratigraphy of the HI24L block. The geological model of this work

(Figure 2.10) is based on the studies previously mentioned and includes 32 faults that cross the domain. To be more specific, the limits between the geological layers (also called horizons) have been generated using an implicit method first introduced by Mallet (1988). The horizons are represented as isovalues of a scalar field that is constrained to the data (well logs, seismic picks) and interpolated in between. The faults remain explicitly meshed.

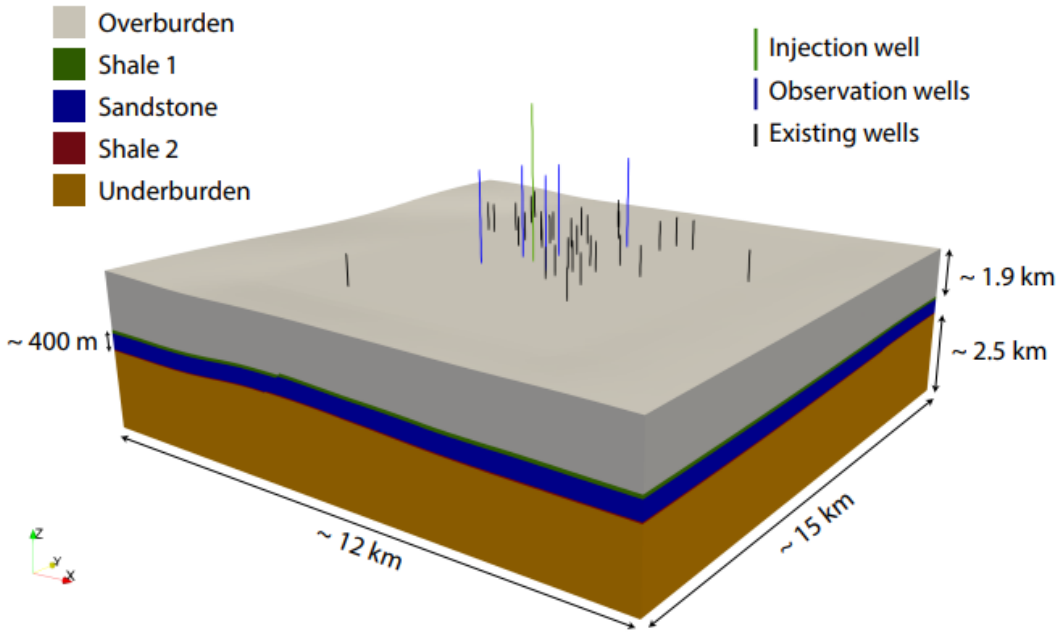

Figure 2.10 High Island domain. The different geological units were interpreted by correlating 3D seismic data and the well logs.

The interval of interest is the Lower Miocene Sandstone, where CO_2 injection will take place. This sandstone reservoir has an average thickness of 400 m and is located at a depth of approximately 1.9 km. We include overburden and underburden layers to properly reflect geomechanical boundary conditions, leading to the model in Figure 2.11. The overburden top is bounded by the seafloor surface and the underburden bottom is limited at a constant depth of 5000 m, far enough below the reservoir to consider it to be a rigid boundary. We use an unstructured mesh with approximately 1.8M tetrahedral cells and 300,000 nodes, leading to 6.3M degrees of freedom - 3 degrees of freedom per cell, and 3 degrees of freedom per node, as explained in the next section. The mesh conforms to the faults and the horizons defining the geological units, allowing for a precise representation of these geometric features. The mesh is illustrated in Figure 2.11, where the reservoir is more refined than the rest of the domain (with a cell size average of 50 m). For modeling purposes, the top two and bottom two layers (overburden, shale 1, shale 2, and underburden) share the same properties and will be referred to as the seal units.

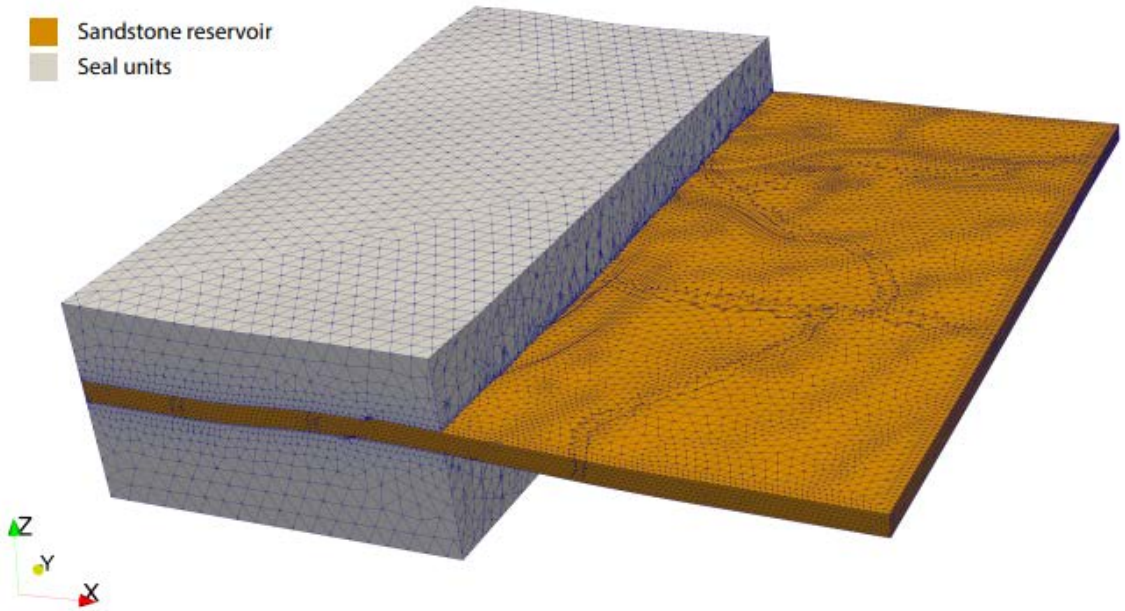

Figure 2.11 Tetrahedral mesh for the reservoir and seal units

Regarding the mathematical model, we consider two components (H_2O and CO_2) flowing in two compressible and miscible phases, namely an aqueous phase and a CO_2-rich phase, in a deformable porous medium. The equations governing the behavior of a deformable porous medium saturated with this fluid mixture under isothermal conditions are given by the balance of linear momentum for the mixture and the mass balance for each component. These equations are supplemented with a variety of constitutive and thermodynamic equations to close the system. The resulting numerical model is implemented in GEOS, and open-source reservoir simulator. A detailed description of the model and specific parameterizations can be found in (Camargo et al., 2022). Figure 2.12, for example, illustrates the heterogeneous permeability field employed.

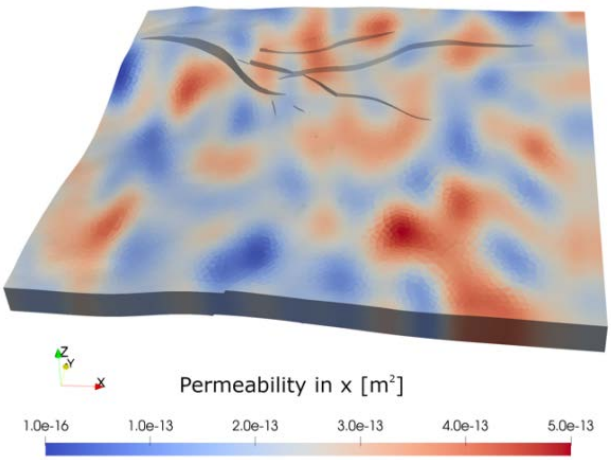

Figure 2.12 Horizontal permeability distribution in the reservoir. The domain has been vertically exaggerated by a factor of 2 for improving the visualization of the faults.

We have simulated the deformation and excess pore pressure distribution after three years of CO_2 injection at a rate of 0.95 Mt/yr, focusing on deformation detectability early in the injection phase. We also investigate the effect of faults on the fluid flow behavior. We evaluate two scenarios. The first one considers that the faults are permeable and do not affect the fluid flow, and the second scenario is the opposite, meaning that faults are assumed to be completely impermeable and act as barriers to flow. No special numerical treatment is used to capture the effects of faults on the solid deformation, such as slip propagation or other contact mechanics. Figure 2.13 illustrates the CO_2 saturation in the reservoir after three years of injection and its accumulation at the reservoir top due to buoyancy. Figure 2.14 shows a side view of the pressure difference between the initial pressure field (before injection starts) and after three years of injection. As expected, the area affected by pressure changes is much greater than the CO_2 plume area. While pore pressure evolves homogeneously when faults are fully permeable, a higher pore pressure magnitude is seen in the vicinity of the injection area when faults act as barriers to flow, given that faults prevent the fluids from migrating to the left side of the domain. A similar pattern develops for the vertical displacements at the sea floor, where the uplift is more concentrated around the injection well and a high displacement gradient is seen close to the impermeable faults (Figure 2.15).

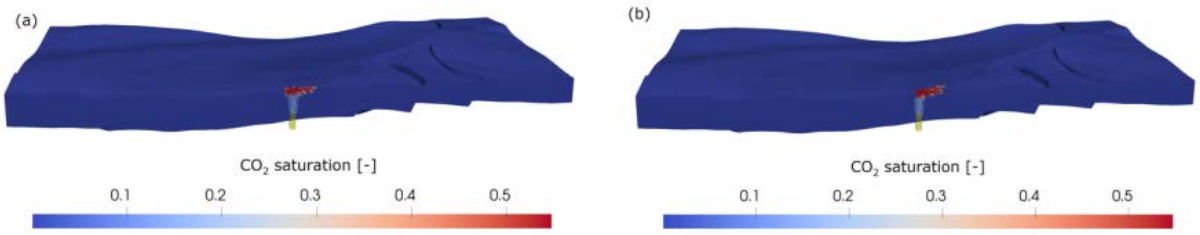

Figure 2.13 Side view of the CO_2 saturation in the sandstone reservoir after three years of injection. Faults are (a) permeable and (b) impermeable. The injection area is illustrated in yellow.

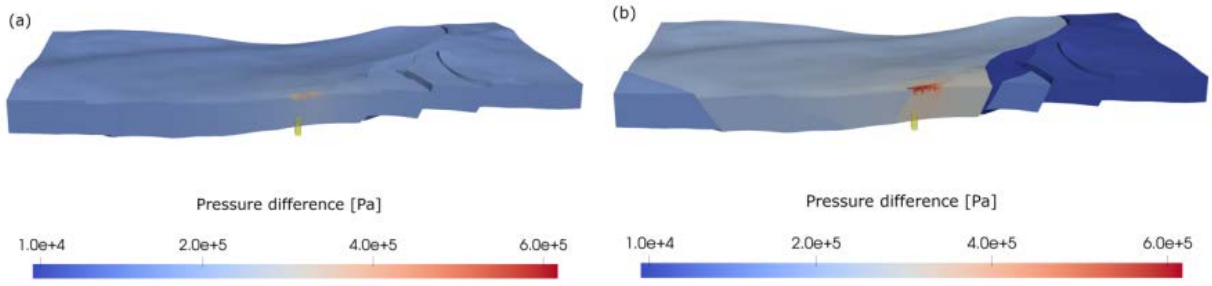

Figure 2.14 Side view of the pressure difference (Pa) in the sandstone reservoir after three years of injection. Faults are (a) permeable and (b) impermeable. The injection area is illustrated in yellow.

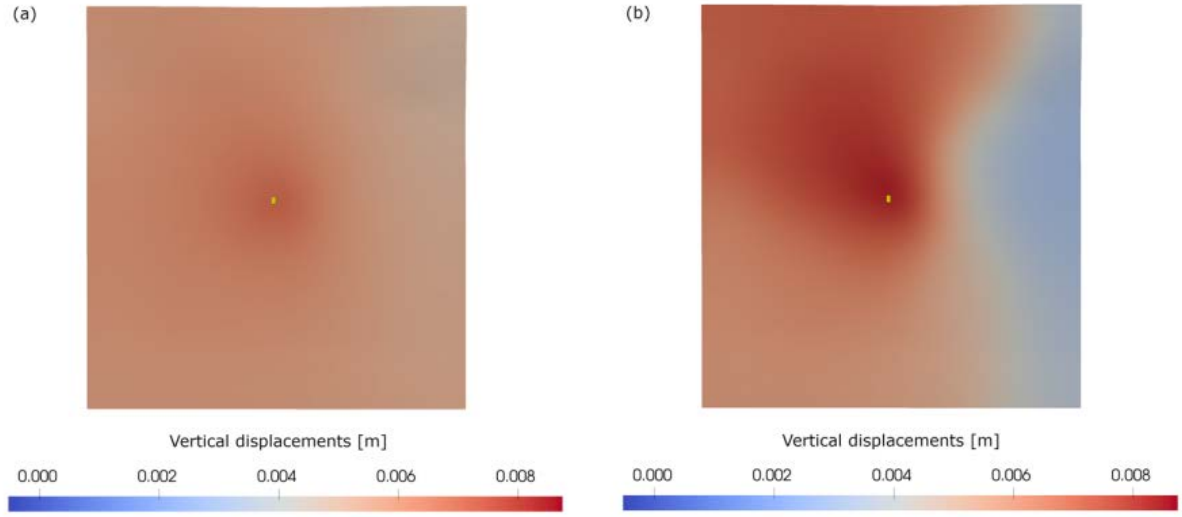

Figure 2.15 Top view of the uplift (m) in the seabed after three years of injection. Faults are (a) permeable and (b) impermeable. The injection area is illustrated in yellow.

Displacements and axial strain along two lines were analyzed for the case in which faults are considered impermeable. The first line is a vertical segment along a hypothetical observation well (light blue dot in Figure 2.16) located one kilometer away from the center of the injection area (dark blue dot). Figure 2.17 shows the results at that point in black, while the dashed vertical line delineates the sensitivity of fiber optic cables and the blue horizontal lines define the reservoir limits. Detectable vertical strains develop in the reservoir, where changes in pore pressure are more pronounced and elastic parameters are smaller compared to the overburden formations.

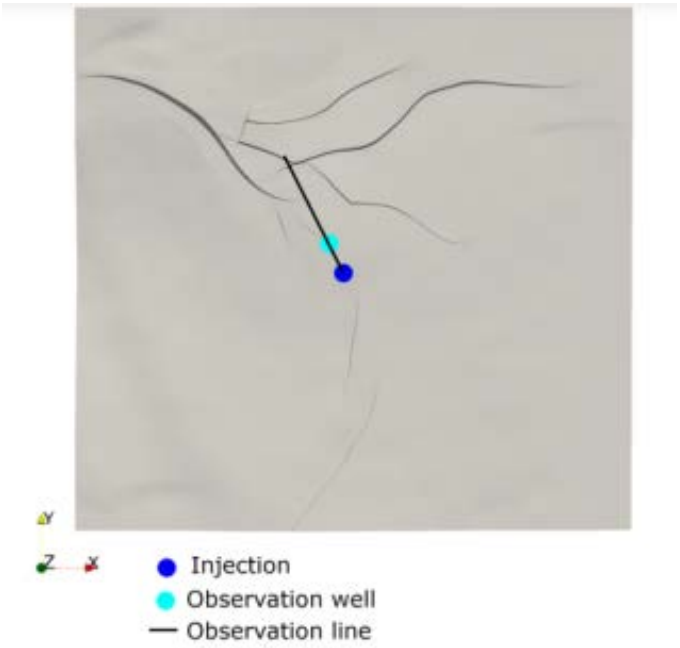

Figure 2.16 Location of injection (dark blue) and monitoring (light blue) well. The location for a line measurement at the seafloor is also shown with a black line.

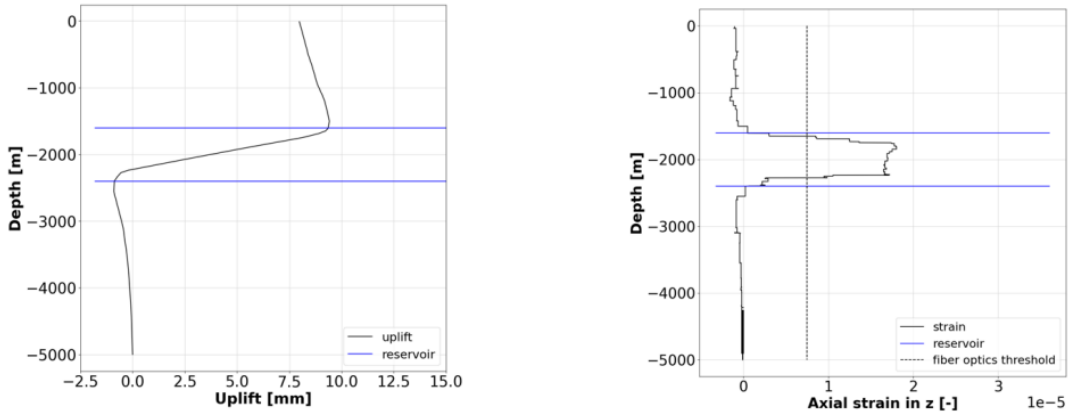

Figure 2.17 Predicted deformation and axial strain on a downhole fiber optic cable in the injection well.

The second line is a horizontal line (black stroke in Figure 2.16) that crosses a fault at the north of the injection area and is oriented in a 27-degree angle with the y-direction. This setup mimics the case where a fiber optic cable is deployed on the seafloor. Figure 2.18 shows axial displacements and strains along the aforementioned line and the vertical red line locates where the line crosses the fault. The plot shows a change in displacement curvature at this point, indicating a change from compressive to tensile strains. Although the axial horizontal strains are too small to be measured by fiber sensors for this particular case, this result suggests that it may be possible to identify the location of faults in the subsurface at some sites by monitoring strains at the seafloor level. We should also note that there is a large uncertainty related to the mechanical properties, and changes in the mechanical properties will directly influence the magnitude of displacements and strains. Future work should capture this uncertainty to provide better informed insights on the deformation monitoring techniques.

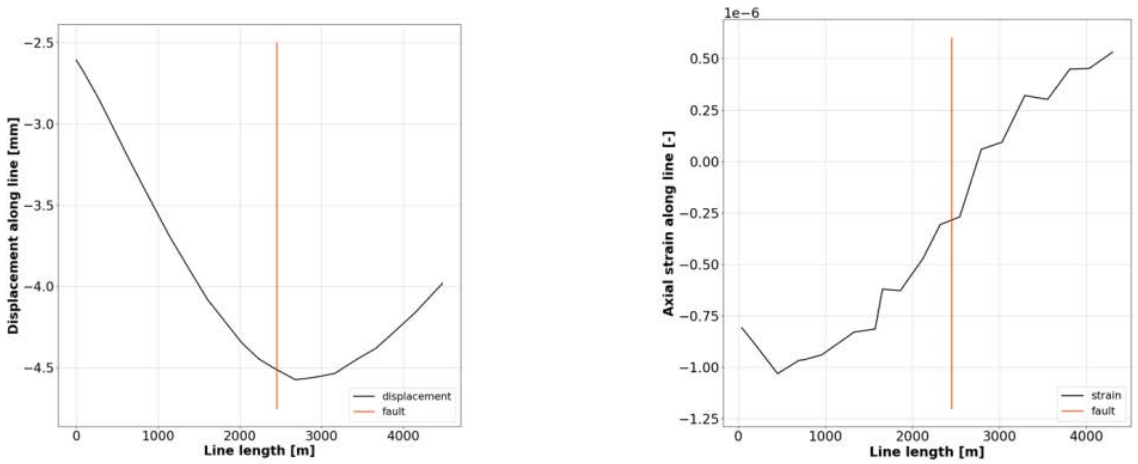

Figure 2.18 Axial displacement (left) and strains (right) along line at the seabed.

Simulation results suggest that ocean bottom pressure recorders have enough sensitivity to detect displacement changes for the whole study area. For strain measurements, fiber optic cables could be deployed to monitor vertical strains along an observation well. The vertical strains magnitudes are

above the detection threshold for fiber optic sensors along the reservoir, but not for the overburden. Table 2.4 summarizes the detection threshold for this site and the maximum value for displacements at the seabed and for the axial strain measured in the vertical well and along the horizontal line.

Table 2.4 Precision of displacements and deformation measurement

Technology	Threshold	Max simulation value
Ocean bottom pressure recorders	1mm for 10 m water depth	11 mm
Fiber optic cables	7.5 µm/m	18 µm/m

The simulations have shown that the excellent injectivity of the reservoir facilitates the dissipation of overpressure, leading to small seabed deformation. Despite the slight uplift magnitudes, ocean bottom pressure recorders are recommended as part of the monitoring system. Their absolute accuracy for the site is estimated to be approximately 1 mm and minimum seabed floor uplift was 2.5 mm. Fiber optic cables are another technology being explored for distributed strain sensing. They can measure strains of the order of tens of micro-m/m and their deployment either horizontally on the seafloor or within vertical wells could provide additional insight. The results have also shown how fault sealing assumptions substantially change the fluid flow and consequently the deformation pattern. Sealing leads to a concentration of excess pore pressure and vertical displacement in the vicinity of the injector well, as well as a noticeable asymmetry in the seabed uplift pattern. As a result, it has been shown that monitoring horizontal strains along the seabed may provide us information about faults location in the subsurface. This preliminary assessment has provided an initial understanding of the reservoir and seal units' behavior. However, many topics may be further explored to increase the reliability of the predictions. In particular, future work will focus on better geostatistical constraints on permeability and porosity, an active area of research for unstructured grids. Additionally, future work should address more detailed analysis of well log data to have a better estimate of anisotropic elastic properties, and more detailed fault seal analysis. Even with detailed structural and geologic information for the site, uncertainties will always remain on the storage reservoir parameters. Therefore, future work should incorporate the uncertainty into the results. Furthermore, it will be interesting to also investigate the reservoir behavior at later injection times (10 to 20 years).

3. Determination of reservoir pressure change based on ground uplift data

Surface and subsurface deformation induced by fluid injection (or production) can be described quantitatively by the framework of poro-elasticity. Once upon knowing deformation, then it is possible to estimate or invert for the pressure change (temporal and spatial) in the subsurface, and vice versus. In addition, even the rock properties and changes (both hydraulic and mechanical) can also be estimated via rock physics inversion or interpretation. The so-called Geertsma solution (Geertsma, 1973) is well known to be applied for this purpose. However, the Geertsma solution has a critical limitation. Namely, the solution can consider only a homogeneous isotropic subsurface, whereas the real subsurface is always heterogenous (e.g., layered) and quite often even anisotropic. Apart from the original Geertsma solution, more advanced analytical solutions are also developed to overcome the limitation but are mostly for isotropic media and/or the number of layers is limited (Du and Olson, 2001; Fokker and Orlic, 2006; Tempone et al., 2010; Mehrabian and Abousleiman, 2015). We may also apply more advanced simulation tools such as finite element, finite difference, etc., which, however, slows down the simulation time.

In SENSE project (WP3), we made important advances that are critical to improve our capability of quantifying subsurface geomechanical behaviours based on ground deformation data. First, we have developed a generalized Geertsma solution that can analyze for the VTI multi-layered subsurface (Park et al., 2021). Since it is an analytical solution, the computational cost is cheap yet provides more realistic modelling opportunities than the original Geertsma solution. Then, by applying the advanced Geertsma, we developed a machine-learning-based inversion algorithm and evaluated the performance with respect to an In Salah-like geological model (Dujardin et al., 2022). Finally, we also made an efficient three-stage inversion framework by which we can invert for not only pressure distribution and mechanical properties, but also fluid saturations (Marin-Moreno et al., 2022). In this section, we summarize all these new developments, while all the details can be found from the three references mentioned above in the current paragraph.

3.1 Generalized Geertsma solution

The analytical solution for displacement field is presented here for an anisotropic layered subsurface subjected to fluid-induced pore pressure disturbance in a reservoir layer (Park et al., 2021). The anisotropy herein refers to a particular case of vertically-transverse isotropic (VTI) stiffness, as shown in Figure 3.1. The analytical solution is derived for a constant pressure change within a reservoir layer, and the pressure change is of cylinder shape, i.e., axis-symmetric problem. The reservoir thickness can be any value, not only infinitesimally small as in Geertsma et al. (1973). In addition, any number of VTI or isotropic layers can be taken into account. Namely, we solve analytically the following axis-symmetric governing equation in cylindrical coordinate (r, z) and Hankel transforms with k being the transform parameter (or wavenumber).

Governing equation:

$$\left[\begin{Bmatrix}\lambda+2G & \cdot\\ \cdot & G_t\end{Bmatrix}\frac{\partial^2}{\partial r^2}+\begin{Bmatrix}G_t & \cdot\\ \cdot & \lambda_t+2G_t\end{Bmatrix}\frac{\partial^2}{\partial z^2}+\begin{Bmatrix}\cdot & \lambda_t+G_t\\ \lambda_t+G_t & \cdot\end{Bmatrix}\frac{\partial^2}{\partial r\partial z}\right.$$
$$\left.+\begin{Bmatrix}\lambda+2G & \cdot\\ \cdot & G_t\end{Bmatrix}\frac{1}{r}\frac{\partial}{\partial r}+\begin{Bmatrix}\cdot & \cdot\\ \lambda_t+G_t & \cdot\end{Bmatrix}\frac{1}{r}\frac{\partial}{\partial z}-\begin{Bmatrix}\lambda+2G & \cdot\\ \cdot & \cdot\end{Bmatrix}\frac{1}{r^2}\right]\begin{Bmatrix}u_r\\ u_z\end{Bmatrix}=-\nabla(\alpha p) \quad (1)$$

Hankel transforms:

$$u_r=\int_0^\infty U_1(z)kJ_1(kr)dk \qquad \text{: radial displacement} \quad (2)$$

$$u_z = \int_0^\infty U_3(z) k J_0(kr) dk \qquad \text{: vertical displacement}$$

$$p = \int_0^\infty P(z) k J_0(kr) dk \qquad \text{: pore pressure}$$

In the equations above, u_r and u_z are the radial and vertical displacements, respectively; p is the pressure anomaly of radius R; ∇ is the gradient operator; (λ, G) and (λ_t, G_t) are the two pairs of the *Lamé* first parameter and shear modulus for the horizontal (or radial) and vertical directions, respectively; α is the Biot coefficient. It is also noted that the *Lamé* and shear moduli are related to the elastic P- and S-wave velocities as below:

$$V_p^2 = \frac{\lambda+2G}{\rho}, V_s^2 = \frac{G}{\rho}, V_{pt}^2 = \frac{\lambda_t+2G_t}{\rho}, V_{st}^2 = \frac{G_t}{\rho} \tag{3}$$

where ρ, V_s, V_{st}, V_p, and V_{pt} are, respectively, mass density, radial/horizontal and vertical S-wave velocities, radial/horizontal and vertical P-wave velocities of each layer. Formally applying the Hankel transforms defined above to the governing equation, we obtain the solution as below:

$$\begin{aligned} U_1 &= \frac{1}{k(\rho V_p^2)} \alpha P + A e^{k_1 z} + B e^{-k_1 z} + C e^{k_2 z} + D e^{-k_2 z} \\ U_3 &= A\phi_1 e^{k_1 z} - B\phi_1 e^{-k_1 z} + C\phi_2 e^{k_2 z} - D\phi_2 e^{-k_2 z} \end{aligned} \tag{4}$$

where:

$$\begin{aligned} \phi_{\pm 1,\pm 2} &= \frac{(V_{pt}^2 - V_{st}^2)\left(\frac{k_{1,2}}{k}\right)}{V_{st}^2 - V_{pt}^2\left(\frac{k_{1,2}}{k}\right)^2} \\ \left(\frac{k_{1,2}}{k}\right) &= \pm\sqrt{\frac{1}{2}\frac{[V_p^2 - (V_{pt}^2 - 2V_{st}^2)]}{V_{st}^2} \pm \sqrt{\left(\frac{[V_p^2 - (V_{pt}^2 - 2V_{st}^2)]}{V_{st}^2}\right)^2 - 4\frac{V_p^2}{V_{pt}^2}}} \end{aligned} \tag{5}$$

In addition, there are four unknown coefficients of A, B, C, and D for each layer, which can be determined by satisfying the interface conditions between adjacent layers (i.e., displacement continuity and traction equilibrium). The related two traction components (S_{rz} and S_{zz}) at the layer interfaces can also be written in the k-z domain as below:

$$\begin{aligned} S_{rz} &= \rho V_{st}^2[(+k_1 - k\phi_1)Ae^{k_1 z} - (k_1 - k\phi_1)Be^{-k_1 z} + (k_2 - k\phi_2)Ce^{k_2 z} - (k_2 - k\phi_2)De^{-k_2 z}] \\ S_{zz} &= +\rho\left[(V_{pt}^2 - 2V_{st}^2)k + k_1\phi_1 V_{pt}^2\right](Ae^{k_1 z} + Be^{-k_1 z}) + \rho\left[(V_{pt}^2 - 2V_{st}^2)k + k_2\phi_2 V_{pt}^2\right](Ce^{k_2 z} + \\ & De^{-k_2 z}) - \frac{\alpha P[V_p^2 - (V_{pt}^2 - 2V_{st}^2)]}{V_p^2} \end{aligned} \tag{6}$$

Once we determine the four coefficients of A, B, C, and D for each layer, we can then obtain the final displacement field in the full-space (r, z) domain by performing numerically the Hankel transforms defined above.

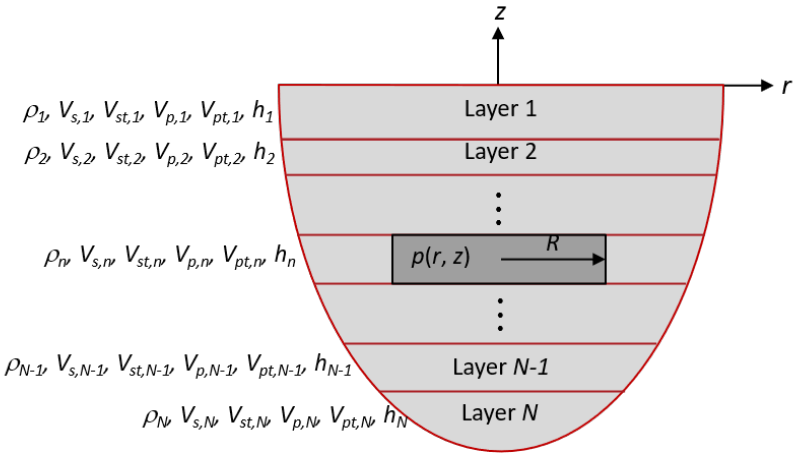

Figure 3.1 VTI anisotropic subsurface model consisting of N layers and subjected to fluid-induced constant pore pressure p(r, z) (darker-shaded) of radius R in an n-th layer. Note ρ, V_s, V_{st}, V_p, V_{pt}, and h are mass density, radial/horizontal and vertical S-wave velocities, radial/horizontal and vertical P-wave velocities, and layer thickness, respectively. Axis-symmetric coordinates (r, z) are used and z-positive is upwards.

The pressure in a real reservoir is typically non-uniform and varies in space (Figure 3.2a). In practice, such distribution can be described via a series of square-cuboid grids. Such a grid can be represented approximately by an equivalent cylinder (or drum) whose volume is the same as the square-cuboid grid (See Figure 3.2b). Then, we can describe arbitrarily-distributed pressure anomaly of any shape by applying the linear superposition of the contribution from as many square-cuboid grids as needed, for each of which we apply the analytical solution presented in the current study and using the equivalent radius (R_{eq}). The linear superposition can be expressed as below:

$$u_{z,i} = \sum_{j=1}^{J} g_{z,ij} p_j \tag{7}$$

where $u_{z,i}$ is the total vertical displacement at point *i*, $g_{z,ij}$ is a vertical displacement at point *i* due to a unit-magnitude pressure anomaly at grid *j* (i.e., so-called fundamental or Green's function), and p_j is the pressure magnitude at grid *j*. When we have the displacement at multiple points (Figure 3.2a), then we can also write the linear superposition expression in the following matrix form:

$$\mathbf{U}_z = \mathbf{G}_z \mathbf{P} \tag{8}$$

with:

$$\mathbf{U}_z = \left[u_{z,1}, u_{z,2}, \dots u_{z,i}, \dots, u_{z,I}\right]^T,$$
$$\mathbf{P} = \left[p_1, p_2, \dots, p_j, \dots, p_J\right]^T, \tag{9}$$

$$\mathbf{G}_z = \begin{bmatrix} g_{z,11} & \cdots & g_{z,1J} \\ \vdots & \ddots & \vdots \\ g_{z,I1} & \cdots & g_{z,IJ} \end{bmatrix}$$

Note that the linear superposition expression in matrix form can also be used for an inversion problem where we invert known (or measured) surface displacement ($\mathbf{U}_z$) to estimate pressure anomaly distribution ($\mathbf{P}$). In this case, it is assumed that the subsurface model (layering and stiffness or the Green's function matrix $\mathbf{G}_z$) is known.

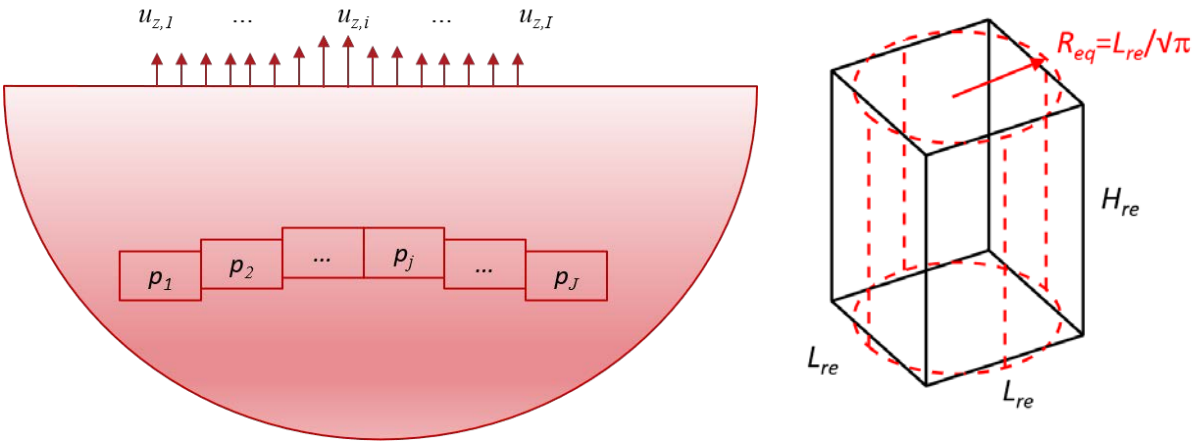

(**a**) (**b**)

Figure 3.2 (a) Schematic description of arbitrarily-distributed pressure anomaly. We assume that the pressure anomaly is discretized into J number of square-cuboid grids, to each of which a value of pressure p_j is specified. The vertical displacement at a point (say $u_{z,i}$) on the surface can be obtained by linearly summing up the contribution from all the pressure grids. (b) Illustration of an equivalent cylinder (radius $R_{eq} = L_{re}/\sqrt{\pi}$) to a square-cuboid of length L_{re}. Note both of the square-cuboid and the equivalent cylinder have the same height of H_{re}.

3.2 Machine-learning-based inversion

We explore the possibility of recovering the pressure distribution in the reservoir from the surface deformation data using a machine learning (ML) approach. We chose to use a convolutional neural network (CNN) with an encoder-decoder architecture as it has proven to be very efficient in the task of pattern recognition. Initially developed in the field of image pattern recognition (Hoeser and Kuenzer, 2020), it has been successfully applied to a variety of tasks in other domains, such as geosciences (Puzyrev, 2019; Xiong et al., 2018). We evaluate our ML approach on a synthetic dataset replicating the measurements from the In Salah CO_2 injection site in the south of Algeria (Bjørnarå et al., 2018). First, we present the synthetic dataset used to evaluate the validity of the ML approach. We then detail the ML network and the generation of the training set, which consists of a series of reservoir pressure distribution maps and their corresponding surface deformation maps computed with the Geertsma's solution (Park et al. 2021). Finally, we evaluate the capabilities of the network on the synthetic dataset and draw some conclusions. We demonstrate that a ML approach can be an effective tool to recover the pressure distribution in a reservoir from the surface deformation analysis. We also highlight the need for a good knowledge of geology and a deep understanding of the shape/dynamic of the data.

Figure 3.3 displays the synthetic model – the base model for our inversion procedure. On the left (input), the synthetic pressure distribution, considered homogeneous over the reservoir height and on the right (output) its corresponding surface displacement computed from finite element (Bjørnarå et al., 2018). In ML terms, this means translating one image to another image. Those topics are best handled using CNN with an encoder-decoder architecture. The ML network is displayed in Figure 3.3. Input data are the surface displacement maps. The encoder is a series of 3 convolutional layers, decreasing the size of the input, but increasing its dimensionality and the decoder is a series of 3 transpose convolutional layers, reducing the dimensionality but increasing the size (the inverse operation). The output is the pressure distribution map. The activation functions through the network are ReLU functions and the network weights updates are made with a classical Adam optimization. The loss function to evaluate the prediction is a mean square error (MSE), to ensure that our trained model has no outlier predictions with big errors.

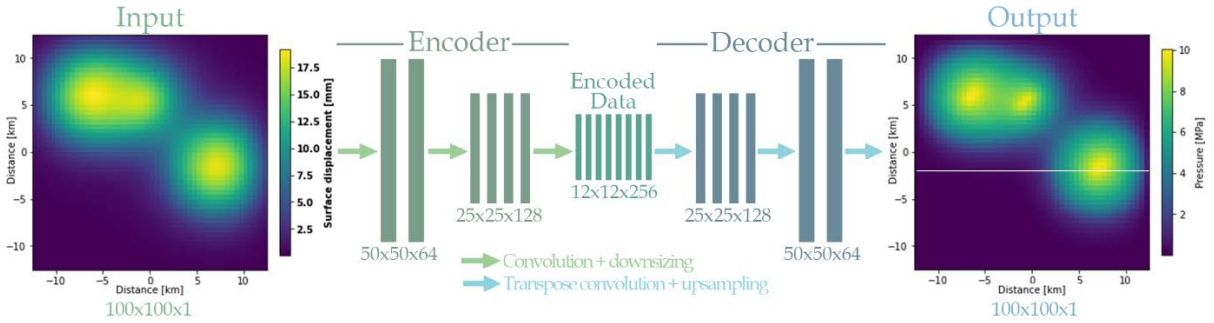

Figure 3.3 Input and output: synthetic data. Output: Pressure distribution in the reservoir. Input: corresponding surface displacement. Middle: ML network composed of and encoder and a decoder. The encoder is composed of three convolutional layers to extract patterns from the input data while reducing the size of the input. The decoder interprets the encoded version by using transpose convolutional layers and up-scaling the data back to its original format.

The generation of the training set requires two steps: creating the pressure distribution maps and computing their corresponding surface displacement maps. The latter is described first in the following. The surface deformation is calculated with the Geertsma's solution (Park et al., 2021). It is an analytical solution that computes a 1D surface deformation response for a given axisymmetric tabular geological model. Each layer is defined by its thickness, its Poisson ratio and its Young's modulus. The reservoir layer is also given a width (a radius) and a constant pressure within it. The surface deformation is then computed radially, from the centre of the considered reservoir. Complex pressure distribution can be handled by taking advantage of the additive property of the Geertsma's solution. Figure 3.4 illustrates this along a 2D profile. A tabular model with distinctive layers (brown) is defined, and the reservoir is discretized into cells (light and dark green). The influence of each cell on the surface deformation is calculated separately and the final surface deformation is the summation of each contribution.

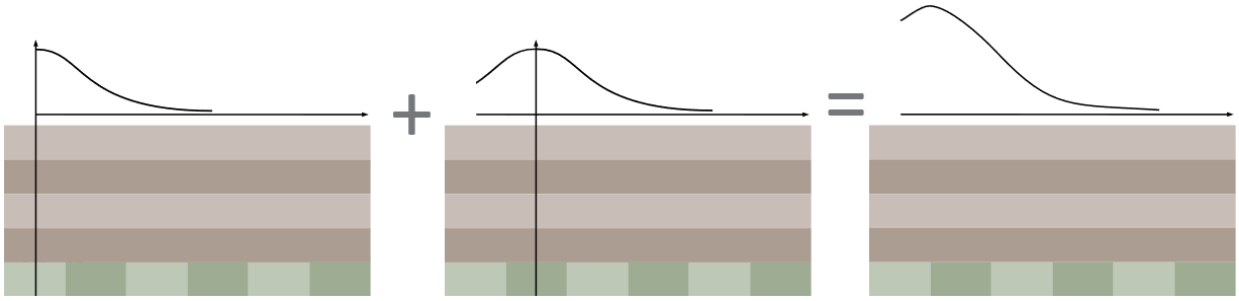

Figure 3.4 Illustration of the additive property of the Geertsma's solution. The contribution of each cell is summed to obtain the final surface deformation.

Next, we consider the pressure maps to be able to train our network. Those maps need to be created with some constraints to create realistic pressure distribution maps with a lot of randomness. Those two constraints ensure that the ML network is learning the mapping between the input and the output instead of returning a bias version of the training set. E.g., a too simplistic pressure distribution in the training set will predict a too simplistic pressure distribution when used on real data. This is a challenging task because it can be dependent on the reservoir properties (homogeneity, anisotropy, etc.), which are not necessarily known prior to the injection. For this study, we observe the synthetic pressure distribution from Figure 3.5 to extract useful properties to create pressure distributions. We observe three patches of pressure on the map. Each one of them as globally a circular shape with a small elongation in one direction (top-right to bottom-left). Next, we display, in blue, in Figure 3.5 the extracted profile corresponding to the white line (Figure 3.3, output) to better understand the dynamic of the data. As a first approximation, the Gaussian curve is a good representation of this pressure distribution (orange line).

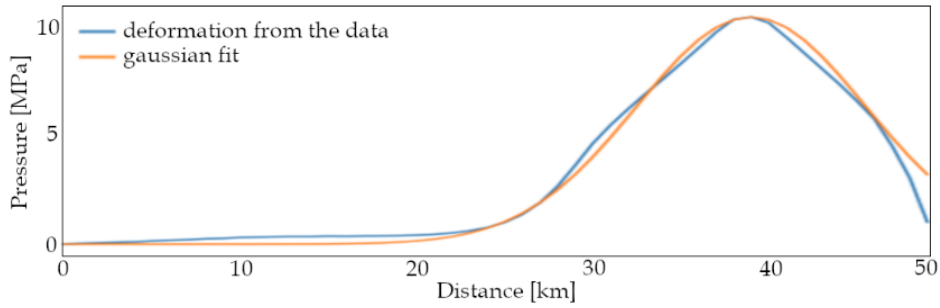

Figure 3.5 The blue line represents the profile of pressure corresponding to the white line on figure 3.3. The orange line is a Gaussian fit of the blue line.

From those observations, we will create the pressure distribution with Gaussian curves in 2D. They are defined by sigma 1 and sigma 2, the location of the centre of the curve, and a rotation angle to avoid only vertical or horizontal elongation. Those four parameters are chosen randomly to create one patch of pressure (Figure 3.6a). We also randomly choose the number of patches we want in one pressure map (Figure 3.6b). Two randomly created pressure distributions are then displayed for illustration in figures 3.6c and 3.6d. It confirms that the properties on the dynamic of the data are respected.

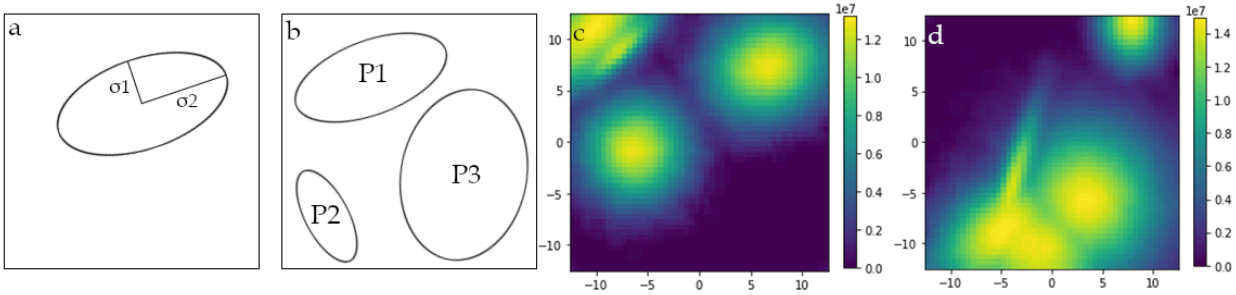

Figure 3.6 (a) and (b): sketches illustrating the procedure to create random pressure distribution. (c) and (d): two examples of pressure distribution randomly created.

The next step is to train the network and assess the results. At this point, the main parameters that can influence the results are 1) how long the network will be trained (epoch number) and 2) the size of the training set. To test those parameters jointly, we do a grid search with the epoch number ranging from 100 to 1000 and the size of training set ranging from 500 to 10000. Figure 3.7 presents (a) the predicted pressure distribution, (b) its associated residual, (c) the surface displacement recalculated for the pressure from (a) and (d) the residual associated with (c). The results are computed with an epoch number of 300 and a training size of 2000.

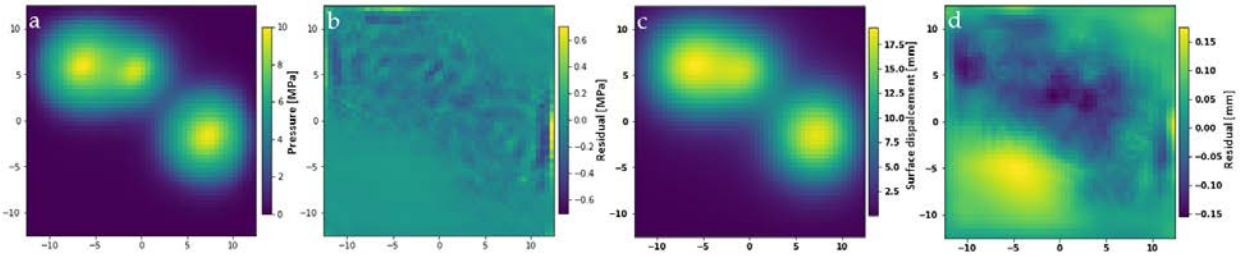

Figure 3.7 (a) prediction of the pressure distribution; (b) residual on the pressure distribution; (c) surface displacement calculated from the predicted pressure distribution; (d) Residuals on the surface displacement.

As we can see, the residuals are quite low, less than 0.5 MPa on the pressure – the maximum pressure in the reservoir being around 10 MPa – which corresponds to an error less than 0.15 mm on the surface displacement – the surface displacement being up to 18 mm. We quantify the error on the predicted pressure distribution using the root mean square error (rmse) value, which in this case is 0.086 mm.

In Table 3.1 all the rmse values are displayed for all the pairs of epoch number and training set size. Those values remain relatively constant for every pairs, which means that the network quickly learns the relationship between the pressure distribution and the surface displacement.

The residuals on Figure 3.7a display a wavy pattern. The same pattern is observed in every prediction (not shown here). The Gaussian curve approximation of the pressure distribution is the cause. The orange curve (Figure 3.5) is a good representation of the blue curve (true data), but the dynamic of those two curves are slightly different, the orange curve is alternatively above (positive

residual) and below (negative residual) than the blue one. This misfit explains the wavy pattern observed in the data.

Table 3.1 RMSE values for the grid search. On top the epoch number is displayed. On the left the size of the training set.

	100	**200**	**300**	**400**	**500**	**600**
500	0.121	0.126	0.096	0.085	0.105	0.098
1000	0.13	0.209	0.136	0.094	0.125	0.104
2000	0.115	0.107	0.086	0.105	0.091	0.068
5000	0.111	0.102	0.102	0.085	0.096	0.082
10000	0.134	0.109	0.147	0.094	0.105	0.079

Further effort should be spent to add more complexity into the training set. In the context of a real-data application, the data preparation can be extensive. Yet, once a ML is trained, it could be used to invert the data without further modification during an injection process, in a time lapse monitoring for example.

3.3 Three-stage inversion approach combined with rock physics modelling

Here we present a methodology to discriminate fluid pressure and saturation changes from surface uplift data by combining an analytical solution for pressure-induced deformation of a multilayered subsurface, machine learning (ML), analytical rock physics modelling, and a capillary pressure model. The methodology consists of the following three sequential stages (or modules) and Figure 3.8 illustrates the workflow.

i) We create a synthetic training dataset of seabed deformations from 1000 three-layer (overburden, reservoir, underburden) models with different elastic properties and pressure perturbations using the generalized Geertsma's solution (Park et al. 2021). We provide the dependency of fluid saturation on seabed deformation by defining the bulk modulus according to an effective media model such as Gassmann (Mavko, 2009). This bulk modulus is changed randomly for different combinations of CO_2 and brine saturations, assuming a sandstone reservoir with constant mineral grain bulk and shear moduli, constant brine bulk modulus and, pressure and temperature dependent CO_2 bulk modulus. We assume that the bulk modulus of the material does not depend on effective stress.

ii) We train a convolutional neural network (CNN) with an encoder-decoder architecture (Figure 3.1) and with the inputs (effective elastic properties and pressure perturbation) and output (surface deformation) from step i). The encoder consists of a series of 3 convolutional layers, decreasing in input size but increasing in its dimensionality, and the decoder is a series of 3 transpose convolutional layers, reducing the dimensionality but increasing in size (the inverse operation). The activation functions through the network are Rectified Linear Units (ReLU) functions and the network weights are updated based on a classical Adam optimization. The loss function to evaluate the prediction is a mean square error (MSE), to ensure that our trained model has no outlier predictions with big errors.

iii) We provide upper and lower bounds of the CO_2 and brine pressures and saturations that can explain surface deformation data by combining several rock physics models (Gassmann, Hertz-Mindlin contact model, Reus effective fluid model; Mavko, 2009) and a capillary pressure model.

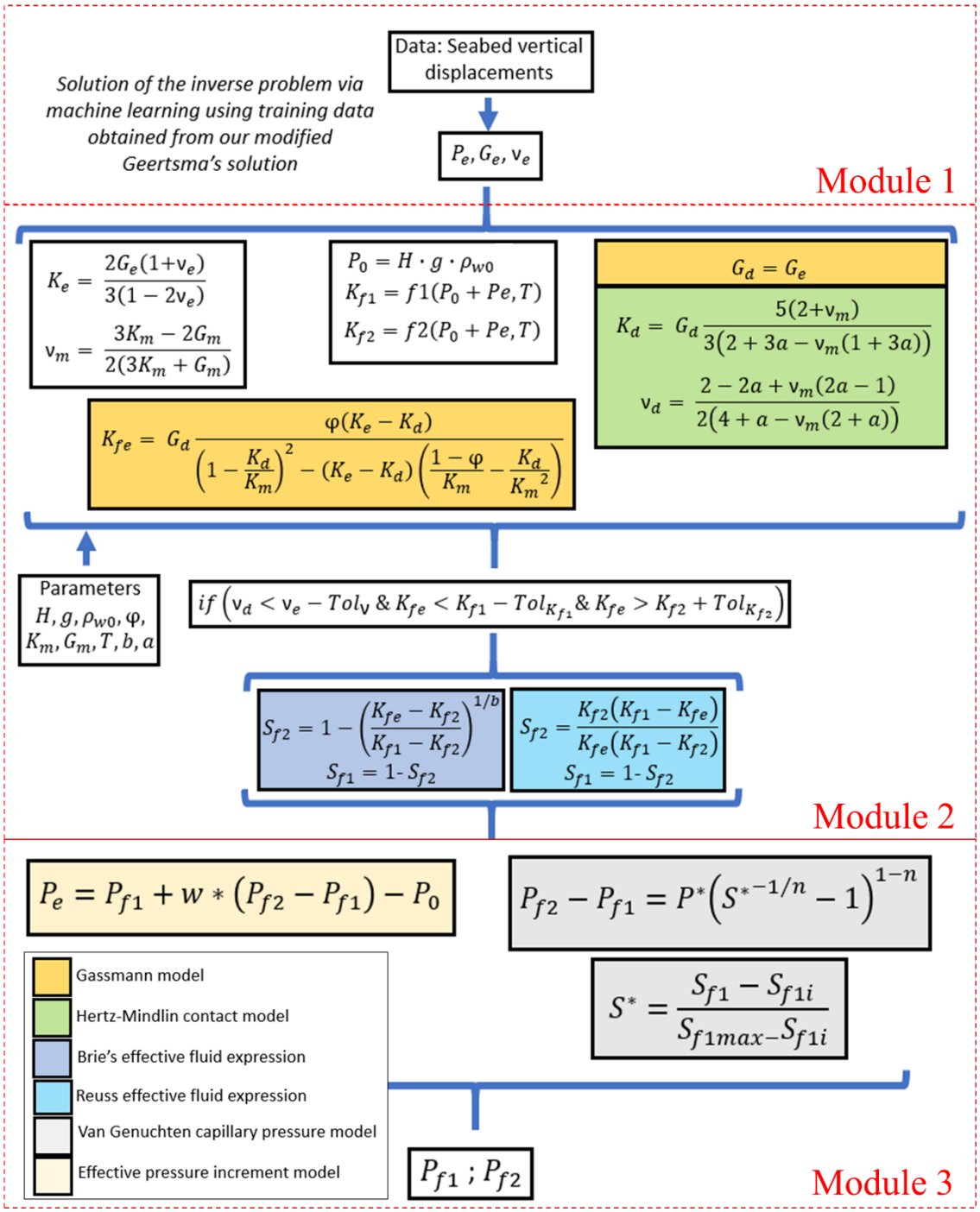

Figure 3.8 Illustration of three-stage inversion workflow.

We test the methodology using seafloor deformation data from a 2D multiphase hydro-mechanical study of geological CO_2 injection, which is introduced into our ML approach. Figure 3.9 shows an example of the brine and CO_2 pressures and saturations estimated from ML results of 2 MPa pressure increase in a sandstone reservoir with an effective bulk and shear moduli of 1.6 GP and 1 GPa, respectively, that explain the input seafloor deformations.

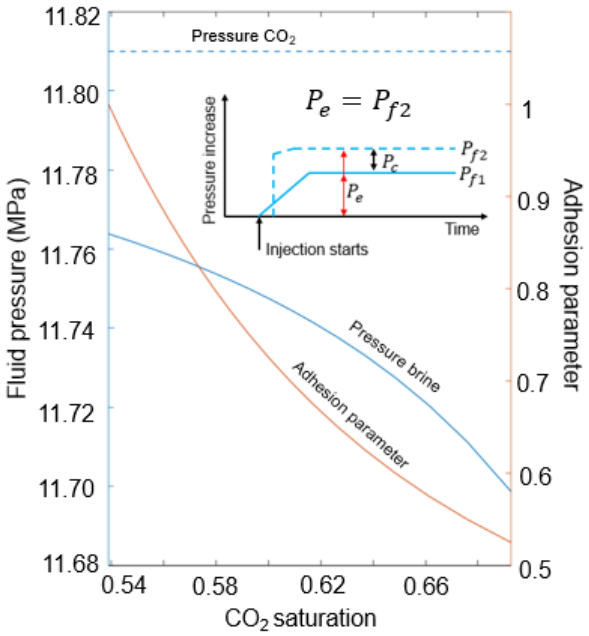

Figure 3.9 Examples of maximum and minimum fluid pressures and saturations explaining seafloor deformation data.

The results in Figure 3.9 consider a model in which the pressure increase obtained with ML is assumed to correspond to the non-wetting phase (in this case CO_2; inset in Figure 3.9). We observe CO_2 saturations ranging between 0.54 to 0.69 depending on adhesion parameter. The adhesion parameter is a free parameter in the Hertz-Mindlin model ranging between 0 (no friction between grains) and 1 (perfect adhesion) (Mavko, 2009). The CO_2 pressure remains constant and the capillary pressure increases with the increase of saturation of CO_2, as expected based on the capillary pressure model. The methodology is applicable for any fluid injection problem where surface deformation data is acquired.

Conclusions

We tested Distributed fiber optics Strain Sensing (DSS) in various settings and environments to find out its resolution and effectivity in measuring small-scale deformations perpendicular to cable axis. Large-scale lab tests, onshore and offshore experiments showed that DSS cables can detect deformations as small as 10 micro-strain, even in noisy offshore environments and when the deformation gradient is high. To prevent influence from the environment and to provide the required coupling to the ground the cables must be trenched and buried in the seabed, about 500 mm cover. Using a steel armoured cable with corrugated outer sleeve, further anchoring to the ground did not improve the sensitivity significantly and is evaluated as obsolete. Although the scaled tests were performed with strain readings at high spatial resolution (some centimetres), less dense readings can probably be used in the field scale, enabling other interrogation techniques based on Optical Time Domain Analysis of Brillouin and/or Rayleigh backscatter to be used. The long-term stability of the readings depends on temperature variations that can be compensated for, and the interrogator itself can also be calibrated if required. Today the interrogators are not suitable for subsea stand-alone operation. However, as the DSS technique allows for measurements over very long distances (20-30 km) the interrogator hardware can in many cases be located topside or onshore. A reasonable approach for offshore CO_2 storage deformation monitoring can be to install DSS cables along CO_2

pipelines or the control umbilical to the injector template, including vertical cable routing along the injector well itself. Quantification of vertical deformation by down-hole DSS measurements in the axial direction of the cable has been thoroughly described by Zhang et al. (2020). A monitoring scheme based on DSS can also be combined with seabed benchmarks that can be utilized for hydrostatic depth surveys and reference measurements. The work presented in this report confirms the feasibility of the DSS monitoring principles. However, more tests and large-scale applications with reference measurements are necessary for better understanding and quantification of vertical ground deformations based on DSS data acquisition. Deployment of DSS cables in trenches (offshore and onshore) and at locations that has deformation potential (faults or barriers) will provide continuous data over the target area and will show if the storage conforms as expected or exhibit anomalies that can trigger other monitoring measures or start an alarm.

InSAR data are readily available over large parts of the world, however, the use of these data for ground monitoring requires heavy processing in order to be used for ground deformation monitoring. We have developed automatic data processing algorithms that can facilitate access to processed data and thus reduce costs for using InSAR data. The processing has been applied to Hatfield Moors natural gas storage site in the UK successfully.

Geomechanical simulation of synthetic and real-life cases with a focus on ground deformation showed that the magnitude and gradient of the observed deformations at e.g., In Salah are well above the threshold for tiltmeter detection limit, while is about the limit of detection for DSS cables. While more expensive than InSAR data, tiltmeter has a higher resolution and will provide good calibration points. Modelling hypothetical cases like offshore Gulf-of-Mexico revealed that with an injection of about one million tons CO_2 per year, a seafloor uplift of about 50 mm might be observed, and it may have a pattern around faults. This level of uplift can be both detected by pressure sensors and DSS cables. Conclusion from the synthetic cases is that the ground deformation caused by injecting CO_2 is usually in a range that can be detected by InSAR and that deformation around features like faults exhibit patterns that may be used to gain more knowledge about sealing or leaking behavior of these features during operation or after decommissioning.

Determination of pressure distribution and plume migration based on the measured ground uplift was also studied. We have developed and verified a semi-analytical solution and an inversion routine that can determine pressure anomaly in the subsurface using ground surface heave as input data. Fast analytical solution of surface heave versus pore pressure change in geological CO_2 storage is a useful screening tool for surface heave monitoring feasibility.

In conclusion, ground deformation can be a useful monitoring parameter. There is a suite of techniques for measuring it onshore (InSAR, Tiltmeter, DSS fiber optics) and offshore (pressure sensors, DSS fiber optics). Deformation observed in our models is in a range that may lead to mechanical failure and induce microseismic events. Monitoring ground deformation combined with microseismic monitoring may provide comprehensive data to understand response of reservoir and cap rock to CO_2 injection.

Acknowledgement

This study was financially supported by ACT consortium (EC project no. 691712) by Gassnova - Norway, United Kingdom Department for Business Energy and Industrial Strategy, Forschungszentrum Jülich GMBH, Projektträger Jülich,Germany, The French Agency for the Environment and Energy Management, The United States Department of Energy, State Research Agency of Spain, with additional support from Equinor and Quad Geometrics, Norway.

References

Bjørnarå, T.I., Bohloli, B., Park, J., 2018. Field-data analysis and hydromechanical modeling of CO2 storage at In Salah, Algeria. Int. J. Greenh. Gas Control 79, 61–72.

Bohloli, B., Bjørnarå, T.I., Park, J., Rucci, A., 2018. Can surface uplift be used as a tool for monitoring reservoir performance? A case study from In Salah, Algeria. Int. J. Greenh. Gas Control 76, 200–207.

Bouquet, S., Frey, J., Malinouskaya, I., Estublier, A., & Fourno, A., 2022. Evaluation of surface movement observability and optimization of the monitoring plan through conceptual and coupled flow-geomechanics models. Proceedings of the GHGT-16 conference.

DeAngelo MV, R. Fifariz R, Meckel TA, Trevino RH. A seismic-based CO2-sequestration regional assessment of the Miocene section, northern Gulf of Mexico, Texas and Louisiana. International Journal of Greenhouse Gas Control 2019;81:29-37.

de Dios, J. C., Delgado, M. A., Martínez, C., Ramos, A., Álvarez, I., Marín, J. A., & Salvador, I. (2017). Hydraulic characterization of fractured carbonates for CO2 geological storage: Experiences and lessons learned in Hontomín Technology Development Plant. International Journal of Greenhouse Gas Control, 58, 185-200.

Da Veiga, S., 2015. Global sensitivity analysis with dependence measures. Journal of Statistical Computation and Simulation, 85(7):1283–1305.

Deb P., Salimzadeh, S., Vogler, D., Düber, S., Clauser, C., & Settgast, R. R. (2021). Verification of Coupled Hydraulic Fracturing Simulators Using Laboratory - Scale Experiments. Rock Mechanics and Rock Engineering, m. https://doi.org/10.1007/s00603-021-02425-y

Du, J., Olson, J.E., 2001. A poroelastic reservoir model for predicting subsidence and mapping subsurface pressure fronts. J. Pet. Sci. Eng. 30, 181–197.

Fokker, P.A., Orlic, B., 2006. Semi-analytic modelling of subsidence. Math. Geol. 38, 565–589.

Geertsma, J. A basic theory of subsidence due to reservoir compaction: The homogeneous case. Trans. R. Dutch Soc. Geol. Min. Eng. 1973, 28, 43–62.

Hawkes, C.D., McLellan, P.J., Bachu, S., 2005. Geomechanical factors affecting geological storage of CO2 in depleted oil and gas reservoirs. J. Can. Pet. Technol. 44.

Herwanger, J., Koutsabeloulis, N., 2011. Seismic geomechanics. How to Build Calibrate Geomech. Model. Using 3D 4D Seism. Data EAGE Publ.

Hillis, R.R., 2001. Coupled changes in pore pressure and stress in oil fields and sedimentary basins. Pet. Geosci. 7, 419–425.

Jimenez, J.A., Chalaturnyk, R.J., 2002. Integrity of bounding seals for geological storage of greenhouse gases, in: SPE/ISRM Rock Mechanics Conference. OnePetro.

Mallet J. Three-dimensional graphic display of disconnected bodies. Mathematical geology 1988;20(8):977-990.

Mehrabian, A., Abousleiman, Y.N., 2015. Geertsma's subsidence solution extended to layered stratigraphy. J. Pet. Sci. Eng. 130, 68–76.

Nordbotten, J.M., Celia, M.A., Bachu, S., 2004. Analytical solutions for leakage rates through

abandoned wells. Water Resour. Res. 40.

Olariu MI, DeAngelo M, Dunlap D, Trevino RH. High frequency (4th order) sequence stratigraphy of early Miocene deltaic shorelines, offshore Texas and Louisiana. Marine and Petroleum Geology 2019;110:575-586.

Paluszny A., Salimzadeh, S., & Zimmerman, R. W. (2018). Finite-element modeling of the growth and interaction of hydraulic fractures in poroelastic rock formations. In Hydraulic Fracture Modeling. Gulf Professional Publishing.

Paluszny Adriana, Graham, C. C., Daniels, K. A., Tsaparli, V., Xenias, D., Salimzadeh, S., Whitmarsh, L., Harrington, J. F., & Zimmerman, R. W. (2020). Caprock integrity and public perception studies of carbon storage in depleted hydrocarbon reservoirs. International Journal of Greenhouse Gas Control, 98(May), 103057. https://doi.org/10.1016/j.ijggc.2020.103057

Park, J., Bjørnarå, T.I., Bohloli, B., 2021. An analytical solution for pressure-induced deformation of anisotropic multilayered subsurface. Geosciences 11, 180.

Ramos, A., García-Senz, J., Pedrera, A., Ayala, C., Rubio, F., Peropadre, C., & Mediato, J. F. (2022). Salt control on the kinematic evolution of the Southern Basque-Cantabrian Basin and its underground storage systems (Northern Spain). Tectonophysics, 822. doi:10.1016/j.tecto.2021.229178

Ruiz I, 2019. Characterization of the High Island 24L Field for Modeling and Estimating CO2 Storage Capacity in the Offshore Texas State Waters, Gulf of Mexico. Master's thesis: The University of Texas at Austin; 2019.

Rutqvist, J., Birkholzer, J., Cappa, F., Tsang, C.-F., 2007. Estimating maximum sustainable injection pressure during geological sequestration of CO2 using coupled fluid flow and geomechanical fault-slip analysis. Energy Convers. Manag. 48, 1798–1807.

Rutqvist, J., Birkholzer, J.T., Tsang, C.-F., 2008. Coupled reservoir–geomechanical analysis of the potential for tensile and shear failure associated with CO2 injection in multilayered reservoir–caprock systems. Int. J. Rock Mech. Min. Sci. 45, 132–143.

Rutqvist, J., Tsang, C.-F., 2002. A study of caprock hydromechanical changes associated with CO 2-injection into a brine formation. Environ. Geol. 42, 296–305.

Salimzadeh S, Paluszny A., & Zimmerman R. W. (2018). Effect of cold CO2 injection on fracture apertures and growth. International Journal of Greenhouse Gas Control, 74, 130–141. https://doi.org/10.1016/j.ijggc.2018.04.013

Salimzadeh S, D Kasperczyk, Z Chen, A Movassagh, E Arjomand, J. Kear (2022), Early Detection of Fault Activation Using Surface Tilt Monitoring During a CO2 Injection Project, 56th US Rock Mechanics/Geomechanics Symposium, 26-29 June 2022 Santafe.

Soltanzadeh, H., Hawkes, C.D., 2008. Semi-analytical models for stress change and fault reactivation induced by reservoir production and injection. J. Pet. Sci. Eng. 60, 71–85.

Streit, J.E., Hillis, R.R., 2004. Estimating fault stability and sustainable fluid pressures for underground storage of CO2 in porous rock. Energy 29, 1445–1456.

Tempone, P., Fjær, E., Landrø, M., 2010. Improved solution of displacements due to a compacting reservoir over a rigid basement. Appl. Math. Model. 34, 3352–3362.

Trevino RH, Meckel TA. Geological CO2 Sequestration Atlas of Miocene Strata, Offshore Texas State Waters. Bureau of Economic Geology, The University of Texas at Austin 2017; report of

Investigations No. 283.

Verdon, J.P., Kendall, J.M., Stork, A.L., Chadwick, R.A., White, D.J., Bissell, R.C., 2013. Comparison of geomechanical deformation induced by megatonne-scale CO2 storage at Sleipner,Weyburn, and In Salah. Proc. Natl. Acad. Sci. 110, E2762–E2771.

Zhang, C.-C.; Shi, B.; Zhu, H.-H.; Wang, B.-J.; Wei, G.-Q. (2020). Toward distributed fiber-optic sensing of subsurface deformation: A theoretical quantification of ground-borehole-cable Interaction. Journal of Geophysical Research: Solid Earth, 125, e2019JB018878. https://doi.org/10.1029/2019 JB018878.